1-19-77

LA-6599-T

Thesis

w

UC-34c

Issued: December 1976

The Measurement of the Elastic Cross Section for Positive Pions on Carbon at 142 MeV

by

Alden T. Oyer

los alamos
scientific laboratory
of the University of California
LOS ALAMOS, NEW MEXICO 87545

UNITED STATES
ENERGY RESEARCH AND DEVELOPMENT ADMINISTRATION
CONTRACT W-7405-ENG. 36

MASTER

This thesis was accepted by the Department of Physics and Astronomy, Graduate School of the University of Wyoming, Laramie, WY 82070, in partial fulfillment of the requirements for the degree of Doctor of Philosophy. It is the independent work of the author and has not been edited by the Technical Information staff.

This work was supported by the US Energy Research and Development Administration contracts E(11-1)-2197 and W-7405-ENG. 36.

Printed in the United States of America. Available from
National Technical Information Service
U.S. Department of Commerce
5285 Port Royal Road
Springfield, VA 22161
Price: Printed Copy $5.50 Microfiche $3.00

TABLE OF CONTENTS

LIST OF FIGURES

LIST OF TABLES

Table Page

CONTENTS OF APPENDICES

ABSTRACT

Alden T. Oyer, The Measurement of the Elastic Cross Section for Positive Pions on Carbon at 142 MeV, Ph. D., Physics, December 1976

A measurement of the elastic cross section $d\sigma/d\Omega$ was made for the reaction $\pi^+ + {}^{12}C \rightarrow \pi^+ + {}^{12}C$ with 142 MeV pions at ten angles ranging from 35° to 85° in the laboratory. This experiment was done at the Los Alamos Meson Physics Facility. A double focusing magnetic spectrometer observed a cylindrical styrofoam target. The resulting momentum spectra were recorded by an array of nineteen totally depleted surface barrier detectors located at the spectrometer's focal plane.

The spectra from the styrofoam were composed of peaks representing proton elastic, carbon elastic, carbon inelastic, and carbon quasi-elastic channels. A function made of Gaussians representing the two body channels and a distribution representing the quasi-elastic channel was fit to the data using a nonlinear least squares algorithm. The ratio of the carbon elastic to proton elastic cross sections was calculated from the areas of the corresponding Gaussians and then multiplied by the proton elastic cross section of Bugg et al eliminating several sources of systematic errors such as beam normalization. The differential cross sections were found to have the usual diffraction structure with a forward peak and a minimum near 55°. Finally, the carbon elastic cross sections were compared to similar $\pi^- + {}^{12}C$ cross sections of Binon et al using the optical model.

CHAPTER I

INTRODUCTION

The use of pions as a probe in studying nuclear structure has been discussed extensively in the literature (KO70, TH70). The primary characteristics are: a) the pion is the primary carrier of the nuclear force; b) the p-wave nature of pion-nucleon scattering at kinetic energies near 180 MeV, with the result that the pion-nucleus interaction depends upon the gradient of the density, and hence is strongly surface peaked; and c) the strong $(\vec{T}\cdot\vec{\tau})$ dependence of the π-nucleon interaction is such that the $\pi^+ + p$ interaction is stronger than the $\pi^+ + n$ interaction (and conversely for π^- scattering). The latter effect and the availability of both π^+ and π^- projectiles may allow one to distinguish neutron and proton characteristics of nuclear wave functions.

These unique physical properties invite investigation for future use. This investigation must attempt to establish a detailed and accurate understanding of the pion-nucleus reaction mechanism. Several theories have been developed to describe this scattering process, but their development was severely hampered by the shortage of reasonable quality data. This was clearly demonstrated by the flurry of theoretical activity (LI76) following the recent publication (BI70) of precise $\pi^- + {}^{12}C$ elastic and inelastic differential cross sections at six energies (120 MeV $< E_\pi <$ 280 MeV). This represented the bulk of the available data where reasonably complete angular distributions have been measured. This dissertation was designed to complement the data of Binon et al by measuring the elastic differential cross section for $\pi^+ + {}^{12}C$ at ten angles at 142 MeV.

A secondary motivation of this experiment concerned the equipment. Except for the substitution of a liquid hydrogen target and the addition of a Cerenkov counter, the same experimental arrangement was used in a more difficult experiment. The differential cross section measurement described in this dissertation provided a means of calibrating and understanding the equipment, and provided assurance the experimental technique was sound.

In measuring an elastic differential cross section, the particles scattered by the target into a given solid angle must be counted. Furthermore, when studying nuclei such as ${}^{12}C$, particles scattered into the inelastic channels must be separated from those scattered into the elastic channel by measuring their momenta with a magnetic spectrometer. One was available in the form of two uniform field magnets arranged in a 180° vertical bend double focusing system. The spectrometer possessed a nominal angular acceptance of 15 msr and a momentum acceptance of ±4.5% of the central momentum. The focal plane was covered by an array of 19 totally depleted silicon surface barrier detectors each 1.0 cm by 3.0 cm by 400 μm and each accepting a 0.5% momentum bite. The path from target to detectors was in vacuum in order to minimize energy loss and multiple scattering effects. A three scintillator telescope located behind the detector array and outside the vacuum system was operated in coincidence with the solid state detectors to provide a particle identification trigger.

The spectrometer's momentum analyzing ability permitted the use of a target material other than pure carbon. This experiment used compressed styrofoam $(CH)_n$ so that a simultaneous measurement of the elastic differential cross sections of $\pi^+ + {}^{12}C$ and $\pi^+ + p$ was made. The latter cross section has been measured in this energy range to 2% by Bugg et al (BB73) providing a basis for normalization. Styrofoam was preferred to polystyrene, polyethylene, and other plastics, as it represented a good compromise between counting rate and energy loss. Also most plastics are unacceptable as they contain oxygen, chlorine, and fluorine, which were unresolvable in this spectrometer. The target was a vertical cylinder whose axis coincided with the rotation axis of the spectrometer.

The pion beam was provided in the Pion and Particle Physics (P^3) area of the Los Alamos Meson Physics Facility (LAMPF). This achromatic channel provided a π^+ beam of 244 MeV/c with a 1.5% momentum acceptance focused into a spot 2.0 cm high by 0.8 cm wide. The beam's vertical size and momentum dispersion dominated the spectrometer's resolution providing an overall momentum resolution of 2.5%. The flux of the beam was measured by an ion chamber located downstream of the target. The beam's transverse position and profile were monitored in real time by two perpendicular multi-wire proportional chambers located upstream of the target.

The data were collected in the following manner. The spectrometer, mounted on a Navy surplus 5 inch gun mount, was rotated to a laboratory scattering angle and the magnets were driven into saturation assuring a consistent starting point on the magnets' hysteresis curve. Then the central momentum was set to observe the upper edge of the spectra by lowering the driving current. Data were collected from all nineteen solid-state detectors for a given amount of beam flux determined by the ion chamber. The central momentum was decreased 3% and more data were recorded. This process of decrementing and recording overlapping portions of the spectra continued until both the carbon elastic and the proton elastic peaks were measured. The spectrometer was rotated and the above was repeated.

The momentum each detector observed was determined from the spectrometer's dispersion, its central momentum, and the detector's displacement from the central trajectory. The counts recorded in each detector were converted to counts per MeV/c by dividing by the effective momentum width of the detector, normalized to a common integrated beam flux, and corrected for the detector channel efficiency. The latter was a mostly geometric effect as the spectrometer's walls prevented the detectors from having a uniform angular acceptance. These efficiencies were determined experimentally by marching the 45° carbon elastic peak across the focal plane in 21 small steps. This procedure also determined the dispersion of the spectrometer.

Each data point had two significant errors. One was caused by the random occurrence in time of the scattering events, a process which was described by a Poisson distribution. Thus, for N counts in a detector, the variance was $\sqrt{N + 1}$. The other error resulted from the uncertainty in the measured detector efficiency. The two errors being statistically independent were summed in quadrature.

Illustrations of the spectra presented in Chapter III show two major Gaussian shaped peaks. Kinematical calculations identified the carbon elastic peak as having greater momentum than the proton elastic peak. Contributions were present from two inelastic and the quasi-elastic channels in carbon. The 4.43 MeV level was not obvious as it lies too near the carbon elastic peak. Similarly, the 9.64 MeV level overlapped the proton elastic peak at the smaller angles. Except at 35°, the quasi-elastic background was underneath the proton peak and extended to lower momenta than were measured. In order to determine the elastic cross sections from the areas of the Gaussians, the contributions from the other channels had to be included in the data analysis.

A nonlinear least squares analysis fit a sum of four Gaussians to the elastic and inelastic peaks and one of two functions to the quasi-elastic background. One of these functions was a step function which was zero above an upper limit. The other was based upon a model devised by R. R. Silbar and M. M. Sternheim (SS76). A kinematical analysis coupled the centroids of the peaks and the quasi-elastic upper threshold to the beam momentum, and linked the broadening of this threshold and the Gaussians' widths to the beam momentum dispersion. Included in this coupling were corrections due to energy loss, straggling, multiple scattering, momentum variation with angle across the entrance of the spectrometer, and the finite beam spot size. The variances of the free parameters (beam momentum, beam momentum dispersion, the areas of the four Gaussians, and the amplitude of the quasi-elastic background) were calculated as part of the fitting algorithm.

The assumed functions fit the data well and provided insight into the validity of the models and into the consistency and reproducibility of the pion beam channel settings. The Gaussians accurately described the two body final states while the step function model proved to have a slightly better fit to the spectrum than the statistical model of Silbar and Sternheim. The pion beam momentum was shown to be reproducible as there was only a slight difference between the beam momentum found for data taken before and after the pion beam was turned off and reset two weeks later. Also, the measured beam momentum was about 2% lower than the value used in setting up the channel.

The determination of the carbon elastic cross section in the center of momentum (CM) system involved the use of the results of Bugg et al (BB73) for the measurement of $\pi^+ + p$ elastic cross section as well as the ratio of the carbon elastic to proton elastic cross section as determined by the present experiment. The pion-proton cross sections of Bugg et al were phase shift analyzed by Carter et al (CA73), and the results for the T = 3/2 channel at 142.9 MeV were used to calculate a cross section for each scattering angle of this experiment. The ratio of the CM carbon to proton elastic cross sections was formed from the ratio of the areas of the corresponding Gaussians. Corrections were made for pion decay in the spectrometer and the unequal number of free protons to carbon nuclei in the target. Having been defined in the laboratory frame, the cross section ratio was transformed to the CM systems by the ratio of the appropriate Jacobians. The carbon elastic cross section resulted from multiplication of the ratio by the extrapolated pion-proton cross section. The final errors of the measurement were a quadrature sum of the variances of the two areas, the uncertainty of the free proton to carbon nuclei ratio, and the error of the extrapolated proton cross section.

The cross sections of this experiment were compared to the $\pi^- + {}^{12}C$ elastic differential cross sections at 150 MeV of Binon et al (BI70) by fitting the data with a complex optical model potential in the Klein-Gordon equation. The charge and matter distribution was taken to be a modified Gaussian, an assumption supported by the shell model and electron scattering data. When fit using either the Kisslinger or the modified Kisslinger potentials, both sets of cross sections agreed within the limits of the optical model thus showing consistency between the two measurements. Although reproducing the general trend of the data, the cross sections calculated from the optical model potential did not accurately reproduce the first diffraction minima. The results of this experiment and of Binon et al (BI70) indicated the minima are deeper and at slightly different angles from those predicted by theory.

The remainder of this dissertation deals with a more complete description of the experiment and an analysis of the results. Chapter II describes the methodology, the equipment, and its calibration. Chapter III details the data analysis including the raw data correction, the functions used to fit the spectra, and the results of the fits. Chapter IV discusses the cross section calculation, the error analysis, and the comparison to the data of Binon et al through the optical model.

CHAPTER II

EQUIPMENT AND EXPERIMENTAL DETAILS

General Overview

Any measurement of the differential cross section requires three elements: a beam of incident particles, a scattering target, and a means of detecting the scattered particle in a given direction. A general overview of the experimental method is presented and is followed by a detailed description of the experimental apparatus.

Facilities for creating pion beams existed at the Los Alamos Meson Physics Facility (LAMPF), and one secondary beam channel, Pion and Particle Physics (P^3), was well suited to the requirements of this experiment. It could supply a beam of either π^+ or π^- in the range of 100 MeV to 600 MeV with a momentum resolution of 1% to 10%. The beam's intensity was great enough to assure a good signal-to-noise ratio and a reasonable counting rate.

Also available was a magnetic spectrometer, which was well suited for observing the scattered pions. Consisting of two bending magnets and an array of solid-state detectors mounted at the focal plane, this device had a well-defined angular acceptance and measured a momentum spectrum of particles having the proper charge and momenta lying within a few percent of the spectrometer's central momentum. Further particle identification could be made from dE/dx information produced by the solid-state detectors, and from a Cerenkov detector which could be added to discriminate against electrons. Information from these two sources was not required by this experiment.

The spectrometer permitted the use of a styrofoam target whose principle constituents were equal numbers of carbon and hydrogen nuclei. The presence of free protons in the target allowed a simultaneous measurement of elastic scattering from both nuclei under almost precisely identical conditions and yielded the ratio $(d\sigma_c/d\Omega)/(d\sigma_p/d\Omega)$ with a minimum of calculation and correction. Having this ratio permitted the calculation of $d\sigma_c/d\Omega$ from the measurement of $d\sigma_p/d\Omega$ by Bugg, Bussey, Carter, Dance, and Smith (BB73).

Data were gathered in the following manner. The spectrometer was set at a scattering angle and the counts from the solid-state detectors were recorded at several successive spectrometer momentum settings. The momentum spectrum at each angle was comprised of peaks from proton elastic, carbon elastic, and carbon inelastic scattering, and a broad distribution from carbon quasi-elastic scattering. A kinematical analysis associated a peak with each scattering reaction; a least squares fit to the data produced the area of each peak. The ratio of the area of the carbon elastic peak to the area of the proton elastic peak yielded $(d\sigma_C/d\Omega)/(d\sigma_p/d\Omega)$.

Three other devices complete this description. An ion chamber (Fig. II-1) located downstream of the target measured the total flux of the beam. A series of scintillators placed in the beam used time of flight to measure beam purity. Two wire chambers produced a real time display of the beam's horizontal and vertical profile, thus assuring that the beam was on target.

The Spectrometer

A side view of the spectrometer system is shown in Fig. II-2. The two 90° bending magnets, having a rectangular gap of 23.7 cm in the bend plane by 9.8 cm, define a solid angle of 15 msr. A set of tungsten slits located at the entry of the first magnet could define a smaller acceptance if needed. The laboratory scattering angle was selected by rotating the entire assembly about a vertical axis centered on the target. The bend was in a vertical plane thus allowing a larger coverage of scattering angles by placing the detectors and spectrometer out of the beam, and minimizing the coupling between momentum resolution and cos θ_L effects. Momentum was set by the uniform magnetic fields and is nominally:

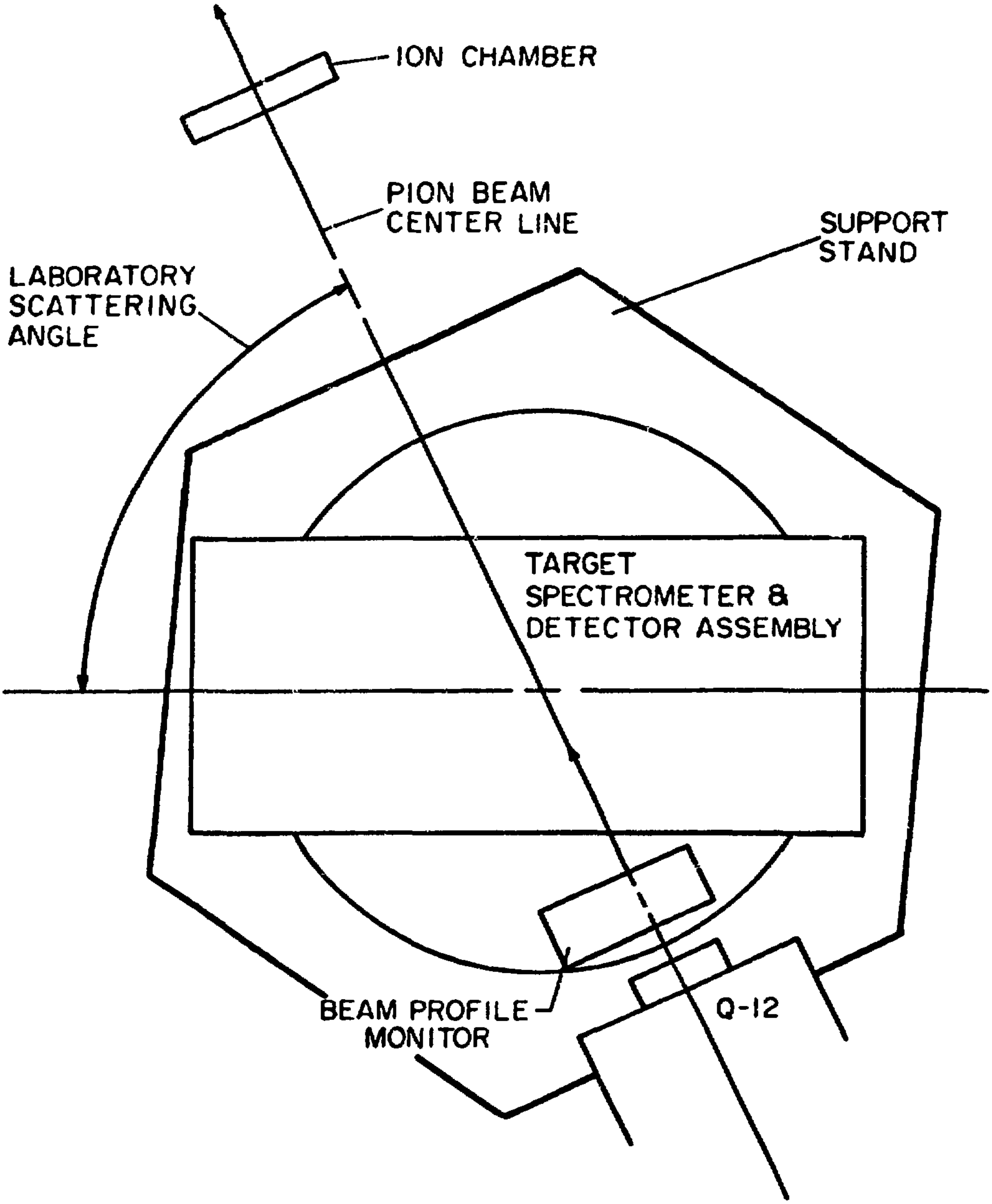

FIGURE II-1. GENERAL EXPERIMENTAL LAYOUT (PLAN VIEW)

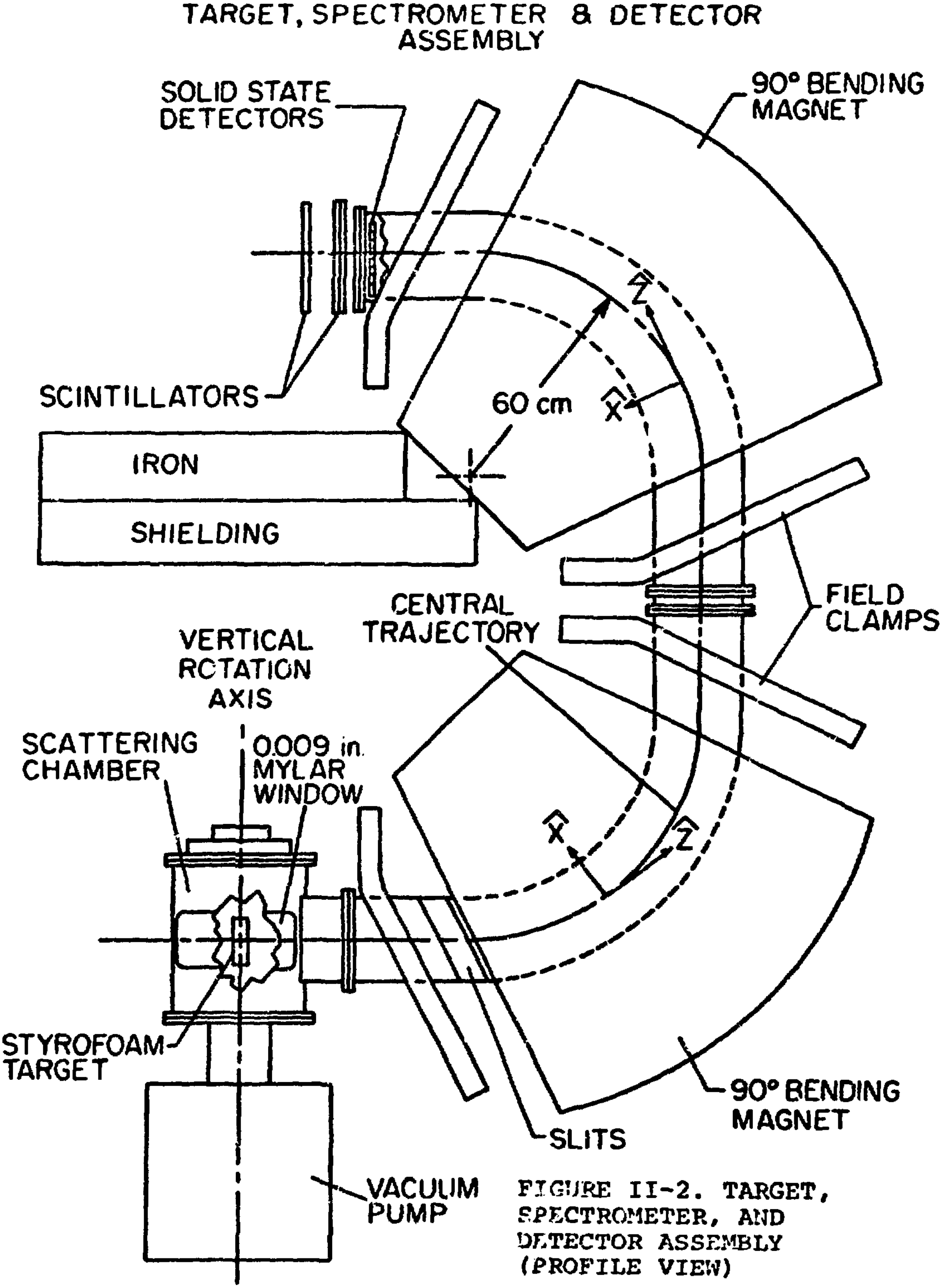

FIGURE II-2. TARGET, SPECTROMETER, AND DETECTOR ASSEMBLY (PROFILE VIEW)

$$pc \approx 0.3rHn.$$

In this relation, r is the average bending radius, 0.6 m, H is the magnetic field in kG, n is the particle's charge in units of the electron charge, and pc is the momentum in MeV. The field, H, was a function of the driving current in the coils. A particle with momentum given by the above, emitted from the center of the target directly into the first magnet, would follow the central trajectory through the system. A particle with slightly different momentum would follow a different path and be displaced at the focal plane. The amount of displacement depended upon the percent deviation of the particle's momentum from the central momentum and the dispersion of the system. Also shown in Fig. II-2 is a set of solid-state detectors which covered the focal plane and measured this displacement. The plastic scintillators operated in fast coincidence, providing a trigger to the solid-state detectors to eliminate background.

The spectrometer was designed using a computer program, TRANSPORT, developed at the Stanford Linear Accelerator Center (SLAC) for the design of their two-mile electron accelerator. It has since been adapted to the computer system at LASL. This code was very general, allowing the user to specify simple bending and focusing fields as well as more complicated effects, such as fringe fields. Furthermore, the program could optimize parameters within constraints set by the designer. Results of a TRANSPORT run were then used as a model for a Monte Carlo simulation that traced particles through the system. This second program calculated the solid angle acceptance and continued the particle past the focal plane and through the scintillator array. Many iterations of this procedure produced the final design of the spectrometer.

One result of this analysis was the use of fringe fields via edge rotation to attain double focusing (focusing in the nonbend plane as well as the bend plane). This is illustrated in Fig. II-2. The entry and exit faces of both magnets were rotated 26.6° off the perpendicular to the central trajectory. The field clamps confined the fringe fields, thus forcing the field's shape to be nearly independent of the central field value.

A series of calibration measurements determined the spectrometer dispersion and calibrated the central momentum as a function of voltage drop (referred to as shunt voltage) across a metal alloy resistor. The first of these measurements was a series of field mappings which established a functional relationship between the shunt voltage and the central field, confirmed the fringe fields were independent of the central field, and demonstrated the uniform field model used in the computer simulations was accurate within 0.2%. The second calibration was done after the magnets were installed in the spectrometer stand. An alpha source in conjunction with two solid-state detectors mounted at the focal plane provided a conversion from kG to MeV/c, and an initial value for the dispersion. The third measurement was made during the experimental run. Using the styrofoam target, a series of 21 measurements was made at 45° with a 244 MeV/c π^+ beam. The sweeping of the carbon elastic scattering peak through all 19 detectors determined dispersion and detector efficiency.

Using identical procedures on both magnets, the fields were measured with one of two devices. A nuclear magnetic resonance (NMR) probe measured the uniform central field to an accuracy of ±1 G. The fringe fields were measured to three figure accuracy with a Hall-effect probe interfaced to a chart recorder, providing a field magnitude versus distance graph. First, the NMR probe was placed on the central trajectory halfway through the magnet, and the magnet was driven into saturation at 1850 A. Decreasing the current slowly in 200 A steps, measurements were made of the central field and the shunt voltage. The results are displayed in Table II-1

To express the data in a compact and accurate form, a least squares fit to the data was made using an integrated Fermi distribution, which was almost linear to a point, and then saturated. The resultant expression is:

$$F(x) = A + B\sigma[1 + \exp(-\mu/\sigma)] \cdot \ln\left[\{1 + \exp[\mu/\sigma]\}/\{1 + \exp[(\mu - x)/\sigma]\}\right].$$

F is the central field in kG, x is the shunt voltage in mV, A is the y intercept, B is the slope at $x = 0$, μ is the point of roll off, and σ is the width of the roll off. A ±3 G error was assigned to each datum due to the uncertainty of the NMR probe and the shunt voltage. The results (displayed in Table II-2) generated the shape of the excitation curve.

The NMR probe was also used to verify the uniformity of the central fields. Magnet 2 was driven into saturation and then set at 1500 A (16.444 kG). Referring to the coordinate system shown in Fig. II-2, displacement of the probe in the radial ($\hat{x}$) direction demonstrated the field was uniform to within 2.5 cm of either coil and increased to 16.447 kG at the coils. Moving the probe parallel to the field lines ($\hat{y}$) showed no change to within the accuracy of the instrument. Measurement along the central trajectory ($\hat{z}$) produced

Table II-1

Magnet Excitation Data

Magnet 1		Magnet 2	
Shunt Voltage (mV)	Central Field (kG)	Shunt Voltage (mV)	Central Field (kG)
6.27	1.762	6.78	1.899
14.53	4.065	14.82	4.138
22.56	6.302	22.79	6.352
30.39	8.491	30.83	8.580
39.05	10.882	39.40	10.951
47.24	13.132	47.50	13.172
55.67	15.386	56.05	15.452
60.09	16.468	60.46	16.543
64.51	17.501	64.54	17.474

Table II-2

Values of Parameters of Integrated Fermi Distribution Used in Magnet Excitation Curve Analysis

Parameter	Magnet 1	Magnet 2
A (gauss)	12.55±8.98	19.65±3.45
B (gauss/mV)	278.9±0.42	277.8±0.15
μ (mV)	74.02±1.13	72.34±0.39
σ (mV)	7.436±0.54	6.484±0.19

no change for 15 cm on either side of center. Operating magnet 1 at 16.613 kG produced identical results. Thus, the central field uniformity was within one part in 10^{-3} exceeding the requirements for 0.5% momentum resolution.

A Hall-effect probe measured the fringe fields of both magnets and produced a graph of the y component of the magnetic field (B_y) versus the distance along the central trajectory from well inside the magnet where the field was uniform to outside the field clamp where the field was zero. Numerical integration of this curve produced two parameters used in TRANSPORT, the effective edge and k_1. The effective edge represents the distance from the edge of the magnet along the central trajectory where the field would drop to zero in an ideal magnet. The parameter k_1 is an adjustment to the transverse focal length due to the gradual fall off of the fringe field. The results are presented in Table II-3.

The effective edge was obtained by numerically integrating the graphs produced by the Hall-effect probe. The total error of the determination was 0.5 cm caused by the uncertainties of the horizontal scale of the graph, the coordinates of the magnet face on the graph, and the numerical integration. The results shown in Table II-3 agree with the expected value of 2.44 cm. The variation with respect to driving current represents a 2 x 10^{-3}

Table II-3

Magnet Fringe Field Parameters

	Current (A)	k_1	Effective Edge (cm)
Magnet 1	364.	.347	2.56±0.50
	764.	.343	——
	1178.	.347	——
	1601.	.354	2.98±0.50
Magnet 2	369.	.336	2.78±0.50
	767.	.337	——
	1177.	.337	——
	1604.	.346	2.15±0.50

variation in the total path length of the system, acceptable for an overall momentum resolution of 0.5%.

The value of k_1 was a measure of the shape of the fringe field and is defined as (BR67):

$$k_1 = \int_{-\infty}^{+\infty} \frac{B_y(z)\,[B_o - B_y(z)]}{gB_o^2}\,dz$$

where B_o is the central field value and g, the magnet gap in the y direction, is 10.795 cm. Results (Table II-3) show a 3% variation between magnets and in each magnet with respect to current. Realizing a 3% error in this determination due to numerical integration and accuracy of the fringe field graphs, one concludes k_1 is the same for both magnets and independent of magnetic field. Subsequent TRANSPORT calculations used an averaged value of 0.343.

The second series of calibrations was made after the alignment of the magnets in the spectrometer stand and the installation of the scattering chamber and the vacuum pump. The source was 1 μCi of ^{241}Am deposited in a 0.1 x 1.0 cm rectangle on an aluminum disk. Its spectrum consists of alpha particles of 5.48574 MeV (85% , 5.44298 MeV (13%), and other energies (2%) (GR71). Tests were run with the source oriented parallel to both the $\hat{x}$ and the $\hat{y}$ axes. The detector was a 0.300 cm thick totally depleted silicon surface barrier detector masked to 0.2 cm ($\hat{y}$) x 1.0 cm ($\hat{x}$) to improve resolution. A screw and bellows arrangement allowed the movement along the central trajectory for several centimeters on either side of the focal plane. A second detector placed 6.35 cm above or below the first was used to estimate dispersion. NIM standard preamplifiers, shaping amplifiers, discriminators, scalers, and bias supplies processed the signals and biased the detectors.

To determine to what degree the model agreed with the spectrometer, the source was oriented with its narrow dimension in the bend plane to yield optimum resolution, and the spectrometer slits reduced the bend plane dimension of the entrance to produce a 7.5 msr acceptance. The resulting spectrum produced two results. First, the main peak was centered on the detector at a shunt setting of 20.125 mV. From the excitation curves, the average field was estimated at 5.617±0.006 kG, producing a conversion factor of 18.01±0.10 MeV/c/kG, which is in excellent agreement with the calculated value of 18.011 MeV/c/kG (a field of 5.617 kG was assumed). Second, the width (full width at half-maximum) of the main peak provided a measure of the system resolution. Its value, 1.8 x 10^{-3}, compares favorably with the value, 1.2 x 10^{-3}, predicted by Monte Carlo simulation - especially when one considers neglected effects in the model were on the order of 10^{-3}.

Orienting the 1 cm dimension of the source along the bend plane to simulate performance with a beam spot of substantial size, the position of the focal plane proved elusive. Spectra recorded over a range of 4.5 cm along the central trajectory were identical, showing a large depth of focus and hence demonstrating the position of the solid-state detector array was not critical. Also, spectra were recorded in the second detector, producing a dispersion of 2.44±0.10 cm/%. This result agrees well with the value of 2.35 cm/% calculated from the TRANSPORT model.

Just prior to the dismantling of the equipment, and after this and another experiment using the same equipment were run, a second run of the alpha source calibration was carried out. The apparatus and procedure were identical to the previous alpha source test, except the source was positioned more accurately with the aid of a surveyor's transit, detectors 9 and 10 of the solid-state detector array were used to detect the emitted alpha particles, and the spectrometer slits were adjusted for full angular acceptance. Setting the discriminators so only the alphas from the main peak were detected, the spectrum was centered upon detector 10 at a shunt setting of 20.001 mV representing a central field of

5.5827±0.0030 kG, and giving a conversion factor of 18.119±0.012 MeV/c/kG. Because it was measured under similar conditions to those of the experiment, this value was used in the data analysis. Besides calibrating the fields in momentum, the series of measurements with the alpha source provided confidence in the spectrometer system and its TRANSPORT model.

The third calibration occurred during the experimental run. Using 19 solid-state detectors, the styrofoam target, a 244 MeV/c π^+ beam, and a spectrometer angle of 45°, the carbon elastic peak was moved across the focal plane in 21 small steps. The spectrum produced in the ith detector was fitted to a Gaussian with mean, μ_i, width, σ_i, and area, A_i.

The mean, μ_i, was the value of the central momentum (that seen by detector 10 which was centered upon the central trajectory) when the scattering peak having momentum P_o was centered on the ith detector. An analysis of the 19 μ_i as a function of detector number, i, produced the dispersion, δ, as defined in the relation:

$$\mu_i = P_o/[1 + \delta(i - 10)].$$

The result of a least squares fit for δ was $(4.924\pm0.023) \times 10^{-3}$ in units of fractional change in momentum per detector as defined above, or 2.285±0.011 cm/%. This was consistent with the results mentioned earlier and represents the best determination of the dispersion.

The efficiency of the channel observed by a detector was proportional to the area of the Gaussian scattering peak, and was chiefly influenced by the spectrometer whose walls shadowed the end detectors relative to the middle devices. Also, variation in the active area, noise, and discriminator adjustment of all detectors contributed to the net efficiencies. Although the former was calculable by a Monte Carlo simulation, the latter must be measured.

A relative efficiency (the ratio of a peak's area, A_i, to some arbitrary value) was sufficient for the data analysis. For convenience, detector 10 was chosen as the reference so the efficiency of the ith detector was A_i/A_{10}. The results are shown in Table II-4. The diminished effiencies due to geometry of the end detectors are evident, as well as the random nature of the other effects discussed above. The unusually large error of detector 1 efficiency resulted from insufficient data being collected on the high momentum side of the peak.

This series of measurements achieved two objectives. First, parameters that are necessary for data analysis (central momentum as a function of shunt voltage, dispersion, and detector efficiencies) were determined and agreed with those calculated from an idealized model.

Table II-4

Relative Efficiencies and Errors of Solid-State Detector Channels

Detector Number	Efficiency	Relative Error
1	0.5840	23.6 %
2	0.6884	7.12%
3	0.7347	2.59%
4	0.8222	2.29%
5	0.9278	2.56%
6	0.9544	4.12%
7	0.9878	3.02%
8	1.0267	2.92%
9	0.8272	2.72%
10	1.0000	3.85%
11	0.8843	3.34%
12	0.8577	4.06%
13	0.8627	4.17%
14	0.8463	4.23%
15	0.8776	2.89%
16	0.5688	3.10%
17	0.7453	2.15%
18	0.6543	5.63%
19	0.6323	7.76%

Second, this established a firm confidence in the accuracy of this model.

Detectors and Electronics

The detector system consisted of two elements: solid-state detectors and scintillators. The 19 silicon devices spanned the focal plane, providing momentum resolution. The scintillators were behind the focal plane and produced a trigger pulse that was used for timing and background discrimination. Thus, a scattered pion within the momentum and angular range defined by the spectrometer passed through one of the silicon detectors and the three scintillators, creating four coincident pulses. This was recognized by the electronics as a bona fide scattering event and was recorded in a scaler. Unwanted background particles from other directions were ignored, since they did not produce this fourfold coincidence. The following discusses the details of this system starting with the silicon devices.

The solid-state detectors were 1 x 3 x 0.04 cm slabs of silicon with the 1 cm dimension being in the dispersion direction ($\hat{x}$), and are mounted on 1.125 cm centers. The large depth of focus allowed a staggered arrangement with the detectors alternately 0.2 cm in front of or behind the focal plane, thus producing an

89% coverage of the focal plane.

The devices were surface barrier diodes of an N-type silicon substrate with a gold layer forming an ohmic contact on the thin P-type layer on the front, and an aluminum layer forming an ohmic contact on the rear. A reverse bias voltage extended the depletion layer to the rear, making the detector's entire volume sensitive to charged particles. The smallest bias required for total depletion was used to prevent breakdown of the rectifying junction.

A schematic diagram of one of the detectors is shown in Fig. II-3. The output of each detector was a current pulse whose total charge was proportional to the energy lost by a particle traversing the detector. This signal was integrated by a transistorized preamplifier that was mounted near the detector to minimize the capacitance of the connecting cable. Its output was an exponentially decaying voltage pulse whose amplitude was proportional to the energy lost in the detector and whose decay constant was 7 μs. After traveling the length of a 100-ft cable, the signal was further processed by a shaping amplifier which amplified, integrated once, and differentiated twice, all of which use a 250 nsec time constant. The result

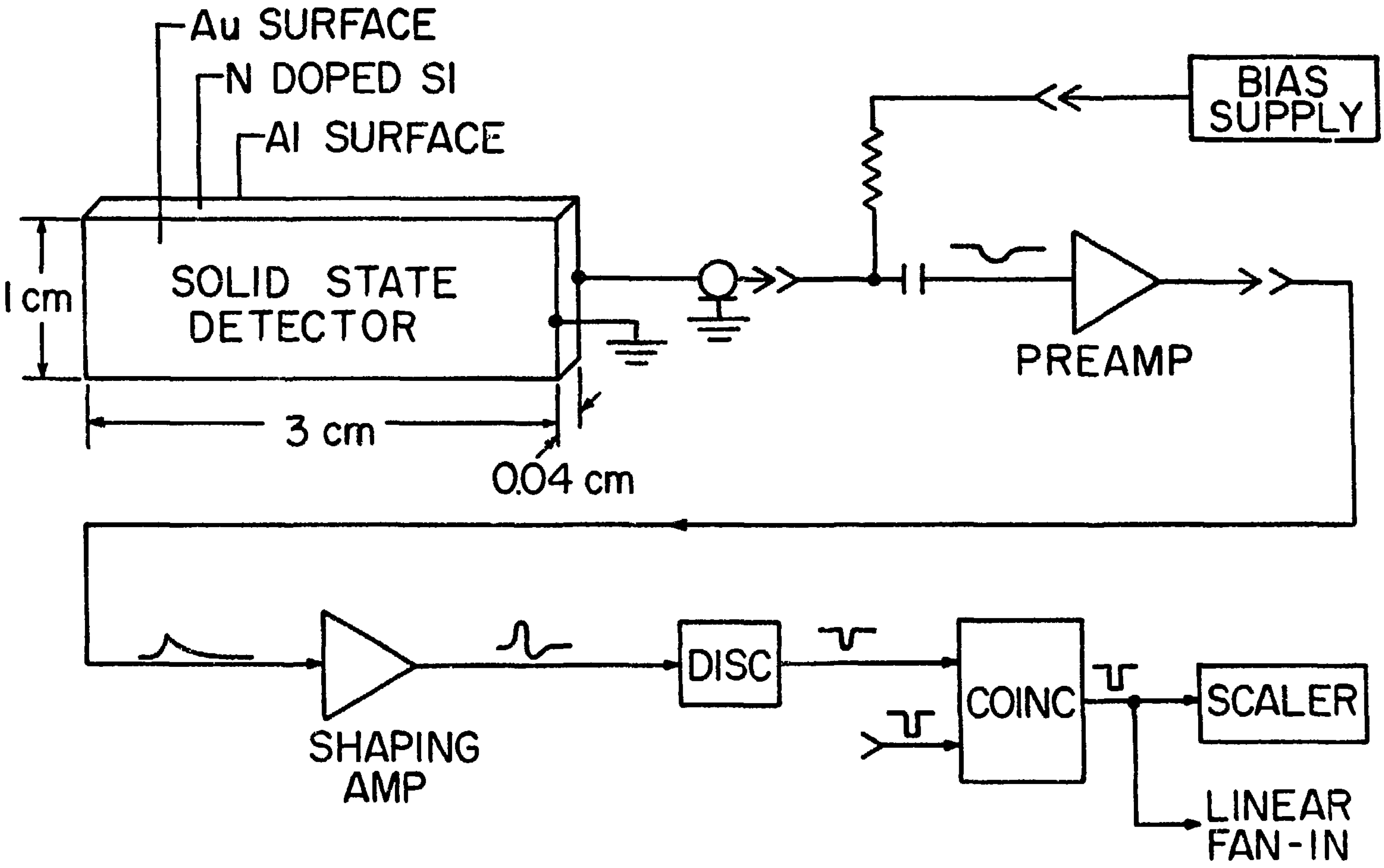

FIGURE II-3.

ELECTRONICS FOR SOLID STATE DETECTORS

was a bipolar pulse with an amplitude proportional to the energy lost in the detector.

The discriminator produced a 20 nsec negative logic pulse if the bipolar pulse amplitude was between two limits. Thus, particles with different energy losses could be differentiated by proper choice of threshold and upper limit. As it was not needed for this experiment, the upper limit was set at maximum and the threshold was set below the expected pulse height, but above the noise level. The discriminator also provided time definition by firing when the bipolar pulse drops to 80% of its peak value. A fast coincidence circuit checked for a coincidence with the scintillator generated trigger pulse. A coincidence signified a bona fide event that was recorded in a scaler.

The scintillators and associated electronics are shown in Fig. II-4. A particle traversing the three 5.7 x 26.7 x 0.5 cm plastic scintillators produced a current pulse in each of the associated photomultiplier tubes which was processed and used as a trigger. Each phototube drove a discriminator whose threshold was set above the noise level. The presence of the three coincident pulses produced a NIM standard negative logic pulse, $S_1S_2S_3$, from the fast coincidence unit and its inverse, $\overline{S_1S_2S_3}$.

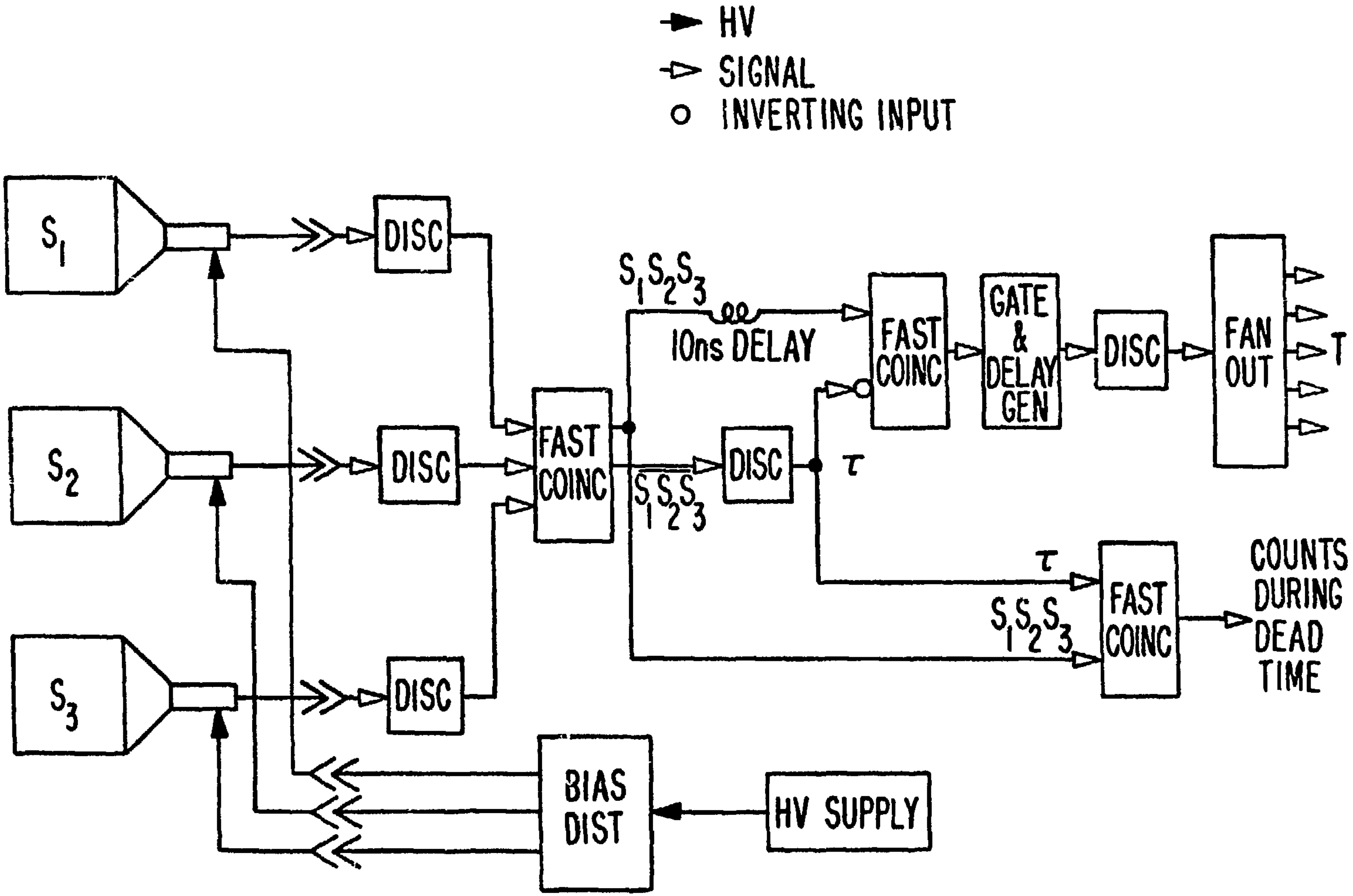

FIGURE II-4.

GENERATOR OF T (TRIGGER PULSE) AND τ (DEAD TIME)

The coincidence pulse, $S_1S_2S_3$, was delayed 700 ns to correspond to the same delay in the solid-state detector amplifier chain, and was lengthened to 250 ns to allow for time jitter in the pulse from the solid-state detectors. Furthermore, the dead time was long enough to inhibit other scintillator coincidences from firing the system until coincidence with the solid-state detectors was complete. This process is illustrated in Figs. II-4 and II-5. The dead time generator was a discriminator that initiated a 1 μs dead time pulse, τ (Fig. II-5d), on the falling edge of $\overline{S_1S_2S_3}$ (Fig. II-5b). Note that there was a 10 ns transit delay in the discriminator. Consequently, $S_1S_2S_3$ (Fig. II-5a) must be delayed 10 ns (Fig. II-5c): τ inhibited further coincidences by driving an inhibit input on a second fast coincidence. An estimate of the number of events lost during the dead time was formed by the coincidence of $S_1S_2S_3\tau$. The trigger pulse, T, was generated from $S_1S_2S_3\overline{\tau}$ by a gate and delay generator, which inserted a delay of 700 ns, and a discriminator that lengthened the pulse to 250 ns. A linear fan out assured that T was distributed without degradation to all imputs.

Some background was eliminated by triggering the scalers only when pions strike the target. The pions

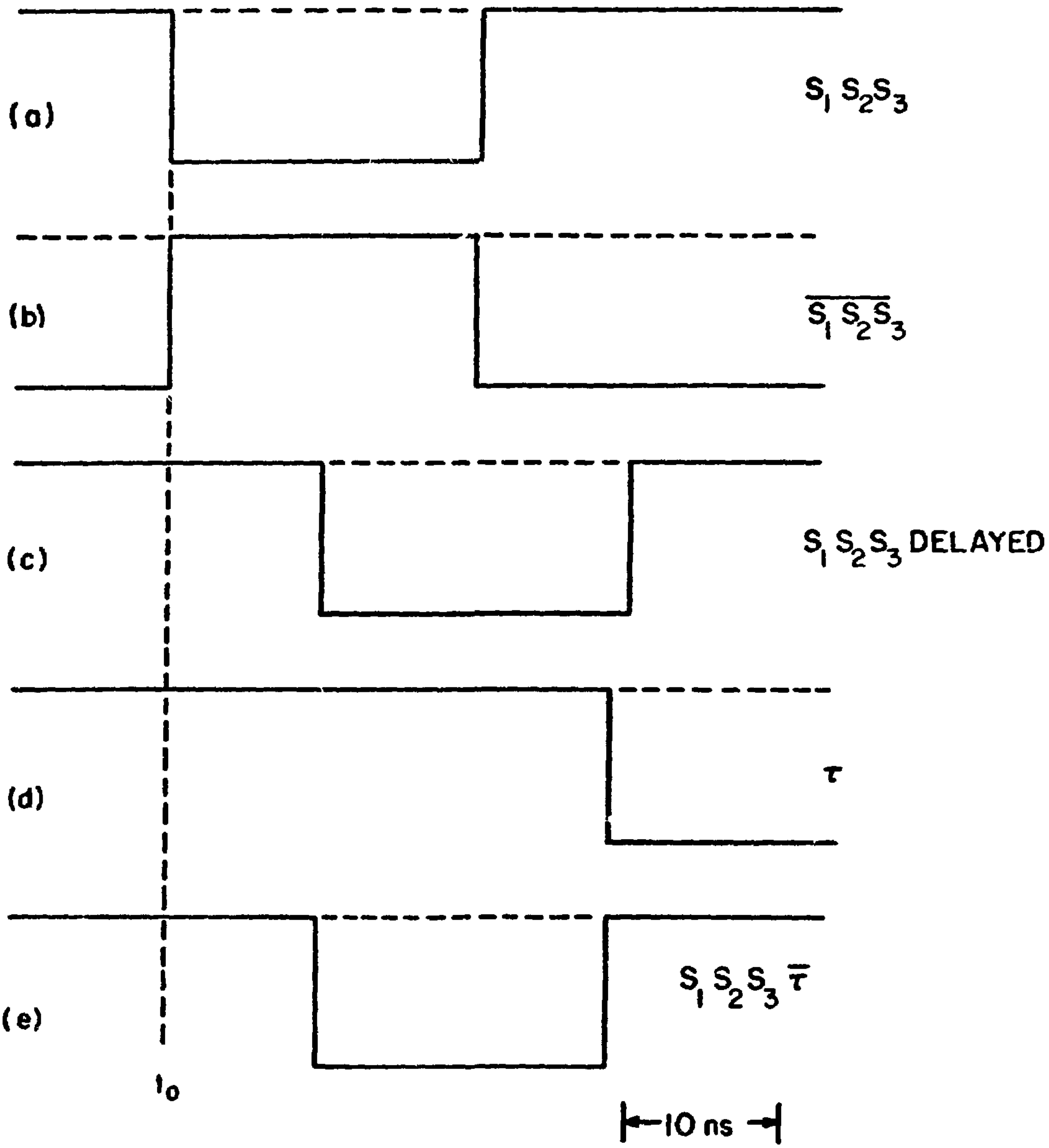

FIGURE II-5.
TIMING PULSES

were produced in clusters of 0.5 ms duration every 8.33 ms. The accelerator generated a logic pulse (beam gate) which was available to the experimenter simultaneous with these clusters. This beam gate drove the enable inputs on the scalers, thus permitting data collection only during target illumination.

Not all triple coincidences resulted from scattering events in the target. A possibly significant number of trigger pulses could be generated from accidental events, which were triple coincidences from uncorrelated events such as cosmic rays, thermal neutrons, and light leaks in the scintillators. For example, suppose a cosmic ray muon was incident at a sufficiently shallow angle to cause a coincidence in S_1 and S_2. If there was a simultaneous pulse from a different source (a thermal neutron, for example) in S_3, the electronics would process this triple coincidence as a real event. Although the equipment could not differentiate between a real and an accidental event, an estimate of the number of accidentals was possible. Because of the random and uncorrelated nature of the process, the two events that produce the triple coincidence would occur simultaneously or at slightly different times with equal probability. Continuing the above example, there was the same probability that a thermal neutron will strike S_3 several nanoseconds before the muon strikes S_1 and S_2. Thus, the accidentals were counted by delaying the output of the S_3 discriminator by 30 ns and testing for a triple coincidence. Typically, one accidental $S_1S_2S_3$ occurred for every 2500 real triggers recorded.

Two other events were of interest. As shown in Fig. II-3, the outputs of the coincidence unit drove a linear fan in. The output of this summing amplifier was a pulse whose amplitude was proportional to the total number of events in the detector array per trigger pulse. This summed pulse was sent to two discriminators. One was set wide open so that it would fire on any pulse. Its output approximated the sum of the total events that are recorded during a data run. The other discriminator's threshold was set at 1.5 times a standard NIM logic pulse amplitude. Thus, it fired only if two or more solid-state detectors showed a simultaneous event.

Finally, all scalers were slaves to a preset scaler that was driven by the ion chamber through a current digitizer, which produced a logic pulse for every 10^{-10}C collected on its input. The preset scaler generated an inhibit voltage when it accumulated a predetermined number of counts. This arrangement inhibited further data collection after a set number of pions illuminated the target, and allowed comparison of one data run with another.

Styrofoam Target

As discussed earlier, the scattering target was styrofoam (foamed polystyrene), because of the equal numbers of hydrogen and carbon nuclei. However, other considerations led to the choice of this material over others such as normal polystyrene and polyethylene (CH_2). Styrofoam could be made dense enough to offer a good compromise between a reasonable counting rate and the effects of momentum loss, straggling, and multiple scattering. It was not an exotic material; it was easily obtained, was easily machined, and did not require an elaborate target holder. Finally, by making the target the same size as a liquid hydrogen target used in later experiments, the styrofoam could be used to simulate the cryogenic target.

"High density styrofoam" as obtained from the manufacturer possessed a density of roughly 0.05 g/cm^3. Increasing the density would increase the counting rate while keeping the energy loss effects within acceptable limits. A hydraulic press failed to compress the material permanently, but baking succeeded. Heating a styrofoam block in a 100°C oven for one hour expanded the plastic to several times its original size. Upon slow cooling, the hot air inside the soft styrofoam cells escaped, and the piece contracted.

Two determinations were made of the density of the treated styrofoam. The first, a measurement involving the entire target, was 0.28 g/cm^3. After the experiment, a second determination was made using only the region of the target illuminated by the beam. Its value of 0.278 g/cm^3 compared well with the first value and demonstrated the density was uniform throughout the target. Fortuitously, the free proton density of the styrofoam was 0.04 g/cm^3, which was only a factor of two smaller than the density of liquid hydrogen. Also, the typical momentum loss in the styrofoam target was 2 MeV/c, a factor of two greater than in the liquid hydrogen target.

Subsequent chemical and spectrographic analysis (performed by the analytical chemistry group, CMB-1, of LASL) determined the chemical composition. The results are shown in Table II-5. The crucial elements, carbon and hydrogen, comprised by weight 89.5±0.2% and 7.74±0.10% respectively, led to a carbon to hydrogen ratio of 0.964±0.013. Oxygen and chlorine presented the greatest contamination and might be apparent only if a detailed study of the first diffraction minima of the carbon elastic cross section was desired. The ash was

Table II-5

Constituents of Styrofoam Target

Amounts are in parts per million by weight unless indicated otherwise. Results preceded by < symbol represent the present limit of detection.

C	89.5 ± 0.2%	Ni	0.9
H	7.74 ± 0.1%	Mn	0.8
O	10000	Cr	0.7
Cl	6000	B	0.3
ASH	1500	Cd	<0.3
Ca	400	Ga	<0.3
Ba	200	Sb	<0.3
Mg	150	Sn	<0.3
P	100	Tl	<0.3
Fe	10	Zn	<0.3
Mo	10	Co	0.2
Si	9	Pb	<0.2
Al	5	Ag	0.1
Na	4	Bi	<0.1
Sr	4	Ge	<0.1
Cu	3	In	<0.1
Nb	3	Li	<0.1
W	<3	V	0.1
K	2	Zr	<0.1
Ti	0.9	Be	<0.01

the material remaining after the sample was vaporized as part of the spectrographic analysis. The other contaminants were negligible.

Pion Channel

A diagram of P^3 is shown in Fig. II-6. An 800 MeV proton beam from the proton linac illuminated a graphite production target where pions and other particles were produced. A three bend analyzing system consisting of quadrupole magnets Q-1 through Q-12 and dipole magnets B-1 through B-3 selected and momentum analyzed either positive or negative pions from the 20° production angle. After the first bend which determined the momentum and polarity of the pions, the beam was focused between Q-4 and Q-5 where a pair of uranium slits define the channel's momentum acceptance. Also a degrader could be inserted to remove protons from a π^+ beam. The second magnet removed off-momentum contaminants and began to make the beam achromatic. A second focus occurred in the center of dipole magnet B-3. This magnet steered the beam to one of two caves, where the last four quadrupole magnets, Q-9 through Q-12, match the achromatic phase space beyond B-3 onto the target of the experiment.

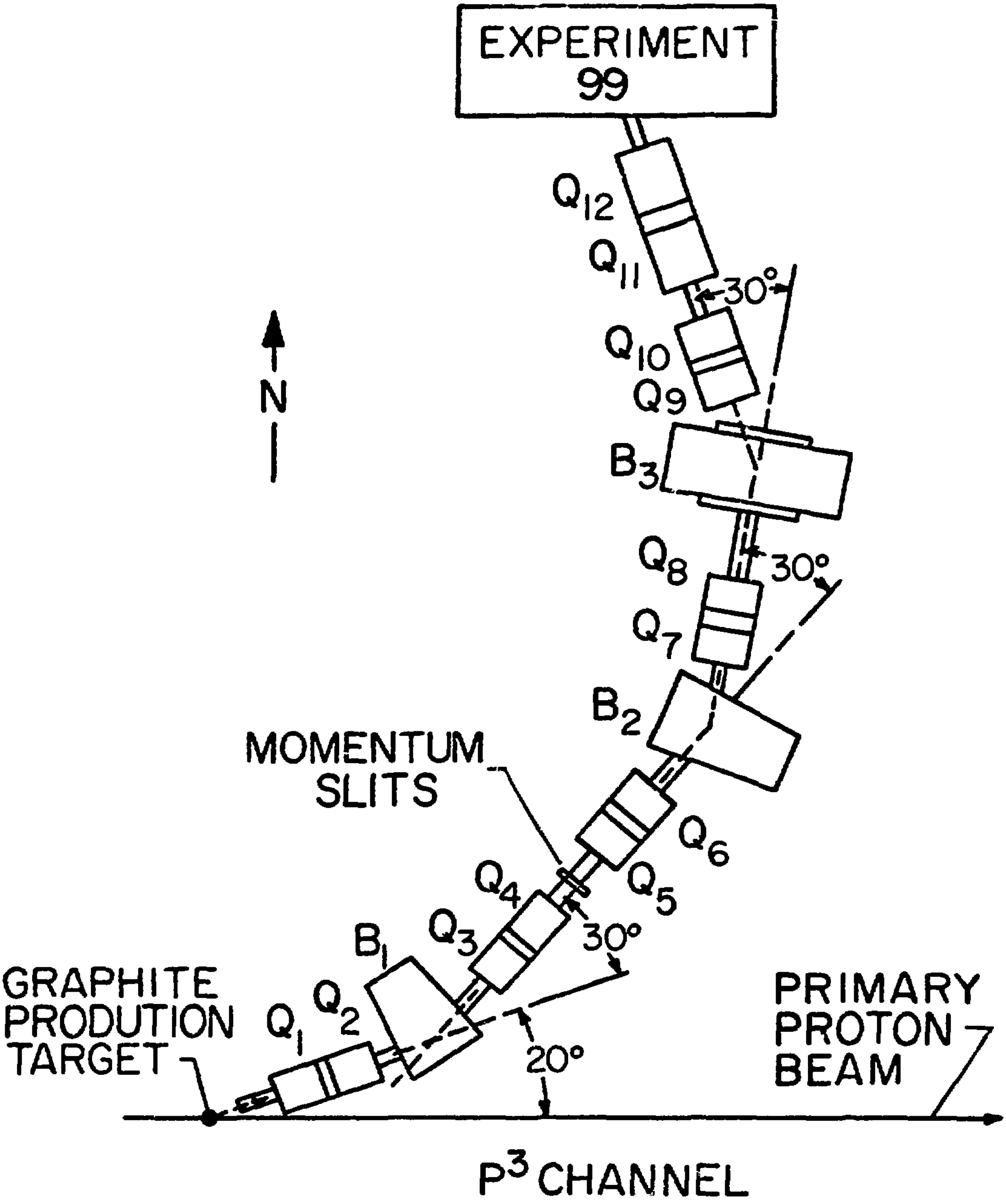
EXPERIMENT 99
Q12
Q11
30°
Q10
Q9
N
B3
Q8
30°
Q7
B2
MOMENTUM SLITS
Q6
Q5
Q4
Q3
30°
B1
Q2
Q1
GRAPHITE PRODUTION TARGET
20°
PRIMARY PROTON BEAM
P3 CHANNEL

FIGURE II-6.

This experiment required a π^+ beam at 250±2.5 MeV/c, having a spot size at the target of 1.2 cm vertically by 0.6 cm horizontally. The channel was tuned from results of computer simulations. The user specified his requirements as input to a TRANSPORT simulation. The resulting magnetic field values were input to a second program, SHUNT, which found the corresponding shunt voltages for the beam line magnets. After the channel was tuned to these values, dipole magnet B-3 was adjusted while observing the profile monitor to place the beam exactly on target.

Beam Monitors

Several beam parameters must be measured and monitored during the course of an experiment. The pion beam momentum and momentum spread were measured indirectly by the spectrometer using a two-body kinematical analysis, and will be discussed in the next chapter. The spot size and position on the target were continuously monitored by wire chamber profile monitors. The total number of pions incident upon the target was measured using an ion chamber. Finally, a scintillator time of flight system determined beam purity.

Two multiwire proportional chambers, located upstream of the scattering chamber (Fig. II-1), produced a real time display of the beam profile in both the horizontal and the vertical directions. The current output from each wire was integrated and then sampled with a multiplexer, producing a beam profile histogram that was suitable for oscillographic display. This arrangement was most convenient for beam tuning and provided assurance that the beam was on target.

The device consisted of both x and y plane wire chambers spaced about 1 cm apart. Each plane contained 64 wires on 0.2 cm centers. The filling gas and bias were not critical; an 80-75% argon, 20-25% carbon dioxide admixture and a -2.8 kV potential produced a a satisfactory output for a beam intensity of 10^5 pions/s.

Figure II-7 shows a block diagram of the electronics for one plane. Each wire, a current source, fed its own amplifier, peak detector, and buffer. The input amplifier converted the current to a voltage and provided some smoothing of the incoming pulse. The peak detector and capacitor held the output voltage's peak value, enabling the multiplexer to scan all 64 wires. The time constant of this stage was sufficiently long to preserve the peak voltage for a complete multiplexer scan. The buffer provided isolation.

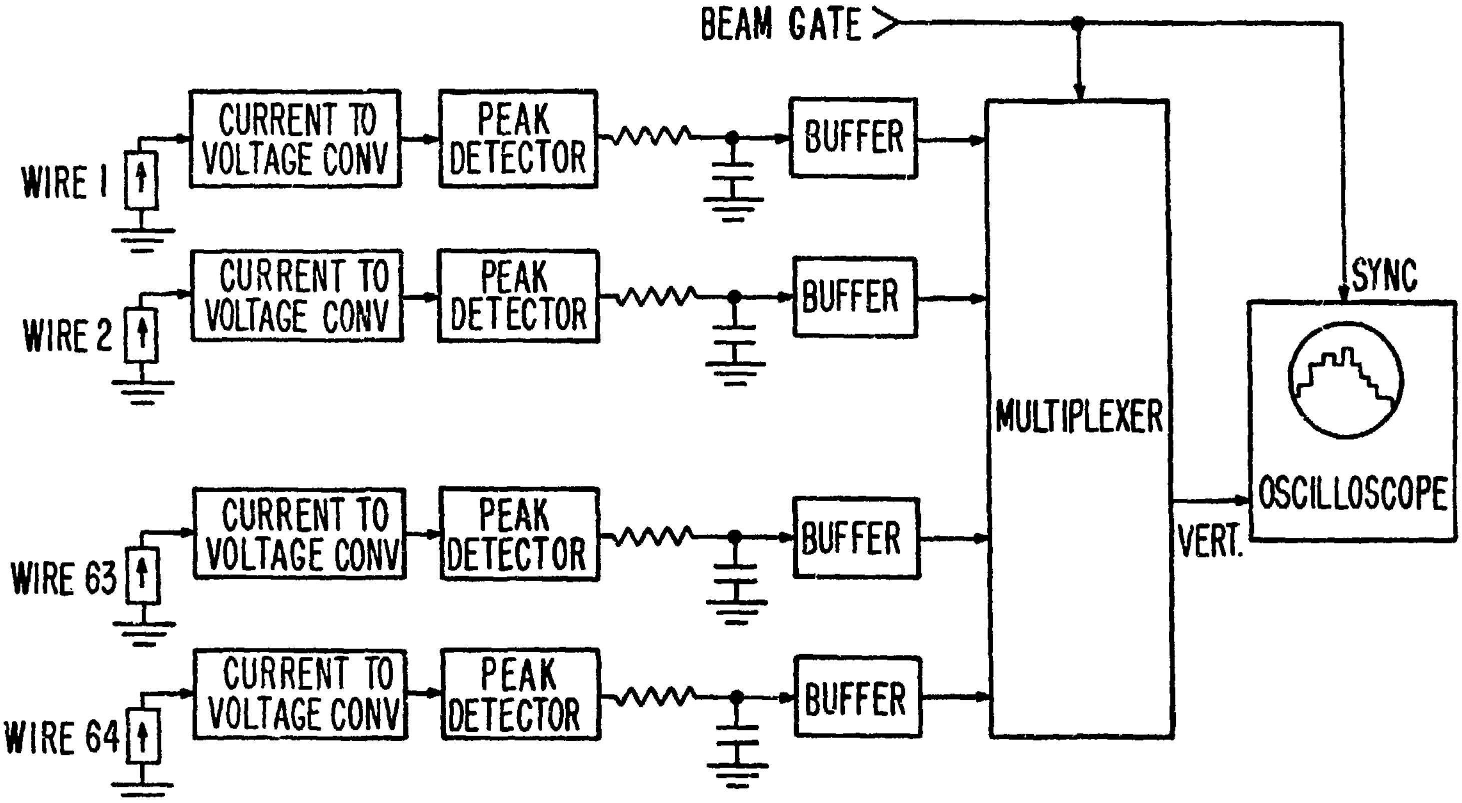

FIGURE II-7.
BEAM PROFILE MONITOR

A beam gate logic pulse initiated a multiplexer scan so the monitor followed any variation of the accelerator's operation.

The ion chamber measured the total flux of the pion beam and terminated data collection, as described earlier. The device consisted of nine 30.5 x 30.5 x 0.08 cm aluminum plates, spaced 2.54 cm apart and mounted in a 43.2 x 33.0 x 25.4 cm aluminum box; dry air was used as the filling gas. The unit was placed downstream of the spectrometer, so that the 0.95 g/cm^2 of aluminum would not affect the beam at the target. The field clamp on the lower spectrometer magnet shadowed the ion chamber for angles forward of 37°. Since the ratio of carbon elastic to proton elastic cross sections was measured by this experiment, ideally, the shadowing had no effect on the determination of the carbon cross section. However, the calibration of the ion chamber was now more dependent upon the steering of the beam.

An absolute calibration of the chamber was desirable but not necessary as long as the device was consistent from one data run to the next. The data analysis discussed in the next chapter supports this assumption. An attempt to calibrate the chamber by counting pions in a low intensity beam failed; the

LAMPF standard scintillators placed in the beam saturated at an intensity too low for the ion chamber to measure.

Beam contamination was measured using a time of flight system comprised of scintillators and a time to analog converter (TAC, a device which produced an analog voltage pulse proportional to the time difference between a start pulse and a stop pulse). A coincidence from a three scintillator telescope mounted with the ion chamber provided the start pulse for the TAC. A signal with an appropriate delay from a scintillator located at the momentum slits in the pion channel was the stop pulse. The output of the TAC drove a multichannel analyzer that recorded the spectra of the pions, muons, and positrons in the beam. The protons, being slowed to 180 MeV/c by the scintillator at the momentum slits, were not transported to the target. Of the three particles, other than protons, 82% were pions, 13% were positrons, and about 5% were muons, the latter being difficult to resolve from the pions. This study shows pions to be the major constituent of the beam. Reactions involving the target and the contaminants are not observed due to the small cross sections of the muons and positrons for the scattering angles observed. Protons scattered by the target would lose all their kinetic energy in the styrofoam and would not be detected. The effect of the contaminants upon the beam intensity is irrelevant as an absolute beam intensity measurement is unnecessary.

CHAPTER III

DATA ANALYSIS

Raw Data Conversion

The transition from raw data to cross section involved three phases. First, the sets of data at each angle were merged into a complete momentum spectrum. Second, a set of four coupled Gaussians plus one of two functions representing the quasi-elastic scattering from carbon were fit to the spectra. Third, the cross sections were calculated from the Gaussians' areas.

The present section describes the raw data, its merge into spectra, and error determination. The next section details the nonlinear least squares algorithm, the fitting function, and the kinematical analysis. The final section discusses the results of the fits. The cross section calculation is considered in the next chapter.

Several sets of data were taken at each angle in order to observe the entire spectrum of carbon elastic and proton elastic scattering peaks. Each data set was generated by setting the shunt voltage to measure part of the spectrum and recording data for a predetermined amount of charge collected by the ion chamber. The shunt voltage was decremented so the spectrometer would observe a lower and overlapping portion of the spectrum and more data were taken. This procedure continued until both elastic peaks were recorded; then the spectrometer was reset to another angle and the process repeated. Thus, for each angle the relevant quantities were the number of events recorded by a detector, the detector number, the shunt voltage, and the total ion chamber charge. These were transformed to two variables, counts per MeV/c and momentum, and errors were assigned.

Two of the independent variables were the detector number and the shunt voltage. The magnet excitation function generated the central momentum from the shunt voltage, and the momentum observed by a particular detector was determined by the detector number and the dispersion using:

$$p_i = P_c[1 + \delta(i - 10)]$$

in which p_i is the momentum of the ith detector, P_c is the central momentum, and δ is the dispersion. The integrated Fermi function and the dispersion are discussed in greater detail in Chapter 2 and Appendix B.

The raw data were counts per detector. Not only must they be converted to counts per MeV/c, they must be corrected for detector efficiency and normalized to the same integrated beam flux. This was accomplished by multiplying each of the raw data counts by a scaling factor defined for the ith detector as:

$$C_{oi} = 4000/(I_c \eta_i P_c \delta)$$

in which I_c is the number of counts from the current digitizer in units of 100 pcoul, η_i is the detector efficiency, and P_c and δ are defined above. The ratio $4000/I_c$ was an arbitrarily selected normalization to an integrated ion charge of 400 ncoul. The factor $P_c\delta$ represents the spacing between detector centers and effects the conversion from events per detector to events per MeV/c.

At this point in the data analysis, only two sources of error were important. One was due to the usual counting statistics. The events occurred randomly in time and were described by a Poisson distribution (RO61). Thus, for N_i events recorded in the ith detector, the absolute variance was $(N_i + 1)^{1/2}$. The other error source was from the efficiency measurement whose errors were generated by the nonlinear least squares fitting routine and were displayed in Table II-4. The two fractional errors are statistically independent and hence were added in quadrature and the result was multiplied by the converted number of events to obtain the absolute variance. Explicitly, the absolute error for the ith detector in units of counts per MeV/c is:

$$\sigma_{ci} = C_{oi}[(N_i + 1) + N_i^2 \xi_i^2]^{1/2}$$

in which ξ_i is the relative efficiency error.

Fitting Routine and Kinematics

The use of Gaussians and a broad distribution to fit the corrected data required the use of a nonlinear least squares analysis. The algorithm used was based upon a method conceived by Gauss (TR57) and adapted to the computer system at LASL (TR74). This method assumed the data, y_i, were described by a calculated function, f, expressable in terms of a set of independent variables, x_j, and a set of adjustable parameters, α_k. A fit was achieved by varying the parameters until the χ^2, defined as:

$$\chi^2 = \sum_i (y_i - f_i)^2/\sigma_{ci}^2,$$

was minimized.

The problem was linearized by considering the initial parameter guess to be a point in a p-dimensional parameter space (p being the number of parameters) and approximating the gradient of χ^2 with respect to α_k by a first order Taylor's expansion. A small step was taken in the direction indicated by the gradient and a new set of parameters was established. The process was iterated until the fractional change of parameters from one iteration to the next was less than 10^{-8}. The variances of the parameters were defined by the square root of the product of the χ^2/N_D and diagonal elements of an error matrix generated by the program and were later used to determine the error of the cross sections.

This method is convenient because any function could be used for f as long as it and its derivatives with respect to the α_j were defined at each data point. The difficulty with any nonlinear least squares analysis was an unfortunate parameter guess could lead to a minimum representing an extraneous solution. However, a careful consideration of the resulting parameters' physical interpretation and a comparison of the calculated function with the data points removed any doubt as to the fit's validity.

Several reactions occurred, including the desired elastic scattering from free protons and carbon as well as a significant contribution from some of the carbon inelastic levels and carbon quasi-elastic scattering whose spectra overlapped those of the elastic channels. The inelastic channels resulted from raising the nucleus from the ground to an excited state. The quasi-elastic process was a reaction leading to a three or more body final state in which the pion freed one or more of the nucleons from the nucleus.

The spectra of the elastically and inelastically scattered pions leading to a two body final state were described by Gaussians as:

$$g_i = A_i(\sigma_i\sqrt{2\pi})^{-1}\exp[(p - \mu_i)^2/\sigma_i^2].$$

The function was normalized so that A_i was the peak's area which is directly proportional to the cross section of the ith channel. The mean momentum, μ_i, and the width, σ_i, were functions of the beam's momentum and momentum dispersion respectively and included corrections for the beam size, the target size, and energy loss and multiple scattering in the target. These modifications will be discussed in greater detail. Only four Gaussians were required, one each for the proton elastic channel, the carbon elastic channel, the 4.43 MeV carbon inelastic channel, and the 9.64 MeV carbon inelastic channel. Although there were other inelastic channels in carbon, Binon et al (BB70) in their measurement of the $\pi^- + {}^{12}C$ inelastic cross sections found contributions only from the 4.43 MeV and 9.96 MeV levels at 150 MeV. Their experiment did not detect any contribution from the 7.66 MeV inelastic channel.

The outgoing pion from the quasi-elastic channel did not have a well-defined momentum as one did for the above two body reactions, but was distributed within some momentum range whose limits are a function of angle for a given beam momentum. The upper limit represented the scattering of a pion which supplied the minimum amount of energy (17 MeV) required to free a nucleon. Inspection of the spectra reveals an approximately flat background whose lower limit was outside of the momentum range measured, thus suggesting a step function which was nonzero below some maximum value. The same effects as for the Gaussians mentioned above broaden the sharp transition of such a function into a smooth curve. An ansatz which describes this is:

$$\mathrm{ERF}(x) \equiv (2A/\sqrt{\pi}) \int_0^x \exp(-t^2)\,dt, \quad x = (p - p_{max})/\sigma$$

in which A is the amplitude, p_{max} is the upper momentum limit, and σ is the broadening of the sharp transition.

A theoretical model for the quasi-elastic process was developed by R. R. Silbar and M. M. Sternheim (SS76) and fit to the data. In this model the Fermi distribution was used to describe the nucleus in which a pion was elastically scattered from one of the bound nucleons knocking the latter free. The cross section for this process was developed from free πN cross sections with allowances made for scattering from within the potential well of the nucleus. It was assumed the pion scatters only once. The resulting momentum spectra of this calculation were presented in tabular form, but could be approximated by the function below. Inspection of the spectra revealed a cusp and suggested the following approximation:

$$g(p) = \begin{cases} AN\{\exp[(p - p_{min})/\tau_1] - 1\}, & p_{min} < p < p_{cusp} \\ A\{1 - \exp[p - p_{max})/\tau_2]\}, & p_{cusp} \leq p < p_{max} \\ 0, \text{ elsewhere} & \end{cases}$$

in which p_{min} and p_{max} are the lower and upper momentum limits, p_{cusp} is the momentum value at the cusp, A is the amplitude of g at the cusp, N is a normalization constant insuring continuity at the cusp, and τ_1 and τ_2 are parameters describing the shape of the exponentials. A typical spectrum is shown in Figure III-1.

The problem stated so far was to fit Gaussians

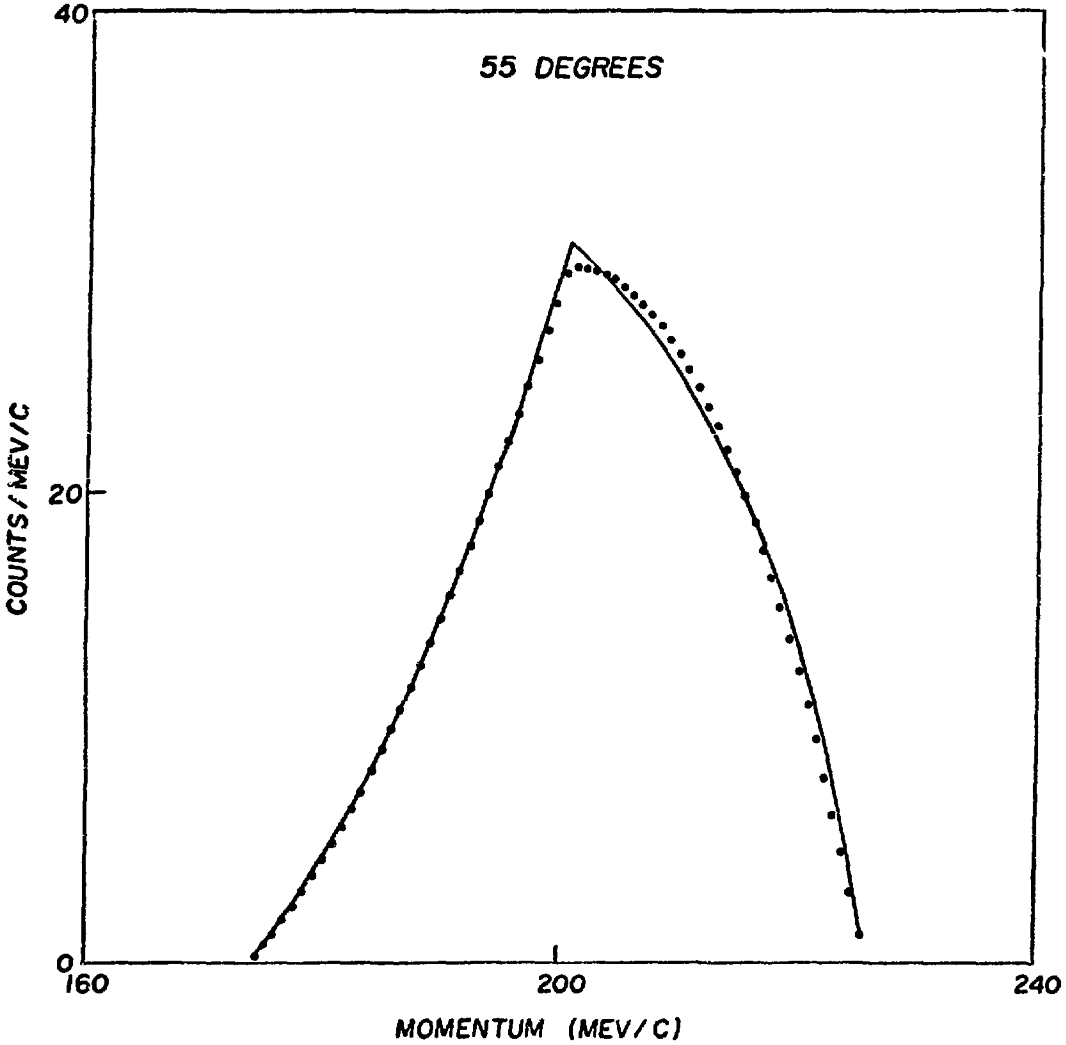

FIGURE III-1. TYPICAL π^+ SPECTRA OF THE SILBAR-STERNHEIM QUASI-ELASTIC MODEL. THE POINTS ARE CALCULATED FROM THE MODEL FOR A BEAM MOMENTUM OF 245 MEV/C. THE CURVE IS THE APPROXIMATION DISCUSSED ON PAGE 55.

to the two elastic and two inelastic channels and a broad distribution to the quasi-elastic channel thus producing fifteen adjustable parameters. Inclusion of kinematics, beam, target, and spectrometer effects reduced the number of free parameters to seven by expressing the centroids of the Gaussians and the upper limit of the quasi-elastic function as a function of the beam momentum, and by expressing the widths as a function of the beam's momentum dispersion. Thus, the free parameters of the fit are the beam momentum, the beam momentum width, the areas of the four Gaussians, and the amplitude of the quasi-elastic function. The remainder of this section details the coupling of these functions. A listing of many of the variables used in the formulae is presented in Appendix A.

The centroids of the peaks and the upper limit of the broad distribution were calculated from two body kinematics using:

$$\mu_i = p_i - p_{loss} - p_{ang}$$

in which p_i is the momentum of the scattered pion calculated from kinematics, p_{loss} is a subtraction due to momentum loss in the target, and p_{ang} represents an angular correction. At a given angle all three quantities were functions of the beam momentum, making the derivative of the fitting function with respect to the beam momentum, p_b, as required by the fitting algorithm, an intricate calculation. To circumvent this difficulty, the following approximation is used. A fixed beam momentum, P_B, is assumed, and the kinematics and corrections were calculated. The fit is run with the above equation redefined as:

$$\mu_i = p_b - P_B + p_i - p_{loss} - p_{ang}$$

in which P_B is the fixed beam momentum used for the kinematic calculations and p_b is the free parameter representing the beam momentum. Different values were tried for P_B until a solution was found where $p_b = P_B$. Then the above equation was correct.

The term p_{loss} was the momentum lost in the target by the pion due to collisions with atomic electrons and was based upon the work of Sternheimer (ST59). The momentum loss in units of cm^2-MeV/c/g was:

$$-1/\rho \; dE/dx = A/v^2 \left\{ \ln \left[\frac{2M_e v^2 W_{max}}{I^2 (1-v^2/c^2)} \right] -2v^2/c^2 - \delta - U \right\}$$

in which I is the target's ionization potential, W_{max} is the maximum kinentic energy transferable to the atomic electron by the incident particle, δ is the density correction, U is the shell correction, and the constant A is:

$$A \equiv 2\pi n e^4/(M_e \rho).$$

The ionization potential of styrofoam was given as 62.92 eV by Jani (JA65), and the density correction was calculated using the formulae of Sternheimer (ST56). In this energy range the shell correction was negligible. The term p_{ang} arose from the finite angular acceptance of the spectrometer over which cosθ is averaged. The spectrometer observed $\overline{\cos\theta}$ but the kinematics were calculated using $\cos\theta_L$. The correction to p_i was:

$$p_{ang} = (\overline{\cos\theta - \cos\theta_L}) \cdot dp_i/d\cos\theta.$$

The beam's momentum dispersion was assumed Gaussian as were the scattering peaks. The two were related by:

$$\sigma_i^2 = (dp_i/dp_b)^2 \sigma_b^2 + \Sigma(\Delta\sigma)^2$$

The first term is the width due to the beam's momentum spread with the derivative being:

$$dp_i/dp_b = (\beta/T_b E_T)(p_b/T_b - \beta\cos\theta_L)^{-1} \cdot [(M_N^2 + M_i^2 - 2M_\pi^2)/2 + (p_i/p_b)\cos\theta_L \cdot (M_\pi^2 + M_N T_b)].$$

The quadrature summation involved other effects including straggling, differing path lengths into and out of the target, the vertical size of the beam spot, the effects of the spectrometer's finite aperture, and small angle multiple scattering. The above expression for σ_i^2 was an assumption justified only by a degree of success.

All the terms of the quadrature summation involved quantities calculated by Monte Carlo computer simulations. One was a simulation of the spectrometer in which a particle randomly generated in the target was traced through the system to the focal plane. This model estimated effects such as magnification and the size of the effective aperture. Using 2 x 10^5 events, the other Monte Carlo simulation estimated the average scattering angle, $\overline{\cos\theta}$, the average path length into the target, $\overline{S_{in}}$, and the average path length out of the target, $\overline{S_{out}}$, and higher order terms. The shape of the beam was assumed Gaussian with a uniform angular distribution. After initially specifying the size of the cylindrical target and the beam's phase space, a random number generator selected a scattering point and directed the particle into a cone slightly larger than the rectangular acceptance of the spectrometer. Rectangular cuts were made of the cone representing the vertical and horizontal sides of the spectrometer as estimated by the spectrometer simulation. If the particle survived the cut, S_{in} was calculated. Then the cone was centered on each of the scattering angles and S_{out}

and cosθ were calculated. These quantities were averaged with the results of previous events and the higher order terms were calculated.

The first of the quadrature terms was a broadening due to straggling which reflected the random nature of momentum loss in collisions with atomic electrons. The mean square contribution was:

$$\overline{S_{out}}\,\rho\,\frac{d}{dx}\,\overline{(p-\bar{p})^2} = \frac{\overline{S_{out}}\,\rho\,2\pi r_e^2 N_o z M_e^2 (1+\gamma)^2}{A[1+(M_e/M_\pi)^2 + 2\,M_e/M_\pi]}$$

in which A is the atomic number of styrofoam.

Variation of path lengths in the target was another source of broadening. Using the higher order terms of the target simulation, the mean square contribution was:

$$\begin{aligned}&\left(\overline{S_{in}^2} - \overline{S_{in}}^2\right)\left(dp_i/dp_b\right)^2\left(dp_b/dx\right)^2\\ &+ \left(\overline{S_{out}^2} - \overline{S_{out}}^2\right)\left(dp_i/dx\right)^2\\ &+ 2\left(\overline{S_{in}\,S_{out}} - \overline{S_{in}}\;\overline{S_{out}}\right)\left(dp_i/dx\right)\left(dp_i/dp_b\right)\left(dp_b/dx\right).\end{aligned}$$

The correction due to the height of the beam at the target was calculated in the following manner. Using the best estimate of the beam spot size from the TRANSPORT solution of the pion channel supported by data from the beam profile monitor, the spectrometer simulation estimated the image's size at the focal plane, and the dispersion converted this quantity into a momentum width. The dispersion being a function of the central momentum was poorly defined after all the data from one angle had been merged, and was approximated for each peak by using δp_i.

The spectrometer's finite angular acceptance introduced a mean square deviation of $\overline{\cos\theta}$, calculated from the target Monte Carlo simulation. This was converted to a mean square momentum variation by:

$$(\overline{\cos^2\theta} - \overline{\cos\theta}^{\,2})\cdot(dp_i/d\cos\theta)^2.$$

The final term in the quadrature sum reflected the effect of small angle multiple scattering as the pion emerges from the target. Using the formalism of Segre (SE53) the mean square contribution was:

$$[\overline{S_{out}}\rho/\chi_o]\cdot[E_s E_i(dp_i/d\cos\theta)\sin\theta_L/p_i^2]^2$$

in which χ_o is the radiation length in polystyrene, and E_s is a constant equal to $M_e\ (4\pi\cdot 137)^{1/2}$.

Results of the Fits

The kinematical results of the fits to the spectra are presented in Tables III-1 and III-2, and the fitted curves are plotted in Figures III-2 through III-11. The solid curve is the best fit to the data. Table III-3, presented as an aid in identifying the various peaks, contains the momenta of the Quasi-elastic upper limit and the Gaussians' centroids. These values were calculated from the beam momenta in Table III-1. However, the beam momenta listed in Table III-2 produced identical values to four significant digits. The two elastic peaks are the most evident features, the proton peak being lower in momentum than the carbon elastic peak. The spectra from the carbon quasi-elastic channel is apparent as a broad distribution beneath the proton peak, especially at 40° (Fig. III-3) and 75° (Fig. III-10).

Special consideration had to be given to the fitting of the 35°, 40°, 70°, 75°, and 85° spectra. At 35°, the normalization of one of the three data sets comprising the spectrum appeared inconsistent with the other two. At this angle only, the field clamp on the lower spectrometer magnet intersected the beam preventing 65% of the pions from reaching

Table III-1

Results of Fit to Data Using Step Function Quasi-Elastic Background

Lab Angle (°)	Beam Momentum (MeV/c)	Beam Width (MeV/c)	χ^2/N_D
35	244.752±0.09	2.25±0.10	3.26
40	244.877±0.05	2.43±0.07	1.70
45	244.311±0.13	2.56±0.11	1.52
50	244.945±0.09	2.80±0.10	1.45
55	244.302±0.10	2.85±0.14	0.65
60	244.817±0.09	2.77±0.15	1.76
65	244.153±0.15	2.94±0.17	1.20
70	244.529±0.11	2.80(FIXED)	1.81
75	244.425±0.16	2.80(FIXED)	1.38
85	244.737±0.13	2.80(FIXED)	1.40

Average Beam Momentum = 244.585±0.036 MeV/c

Average Beam Width = 2.66±0.05 MeV/c

Table III-2

Results of Fit to Data Using Silbar Model Quasi-Elastic Background

Lab Angle (°)	Beam Momentum (MeV/c)	Beam Width (MeV/c)	χ^2/N_D
35	244.743±0.09	2.25±0.10	3.31
40	244.813±0.06	2.53±0.07	2.18
45	244.153±0.13	2.69±0.11	1.63
50	244.868±0.09	2.88±0.09	1.43
55	244.282±0.11	3.02±0.14	0.69
60	244.910±0.10	3.09±0.15	2.03
65	244.338±0.15	2.75±0.19	1.18
70	244.587±0.16	2.80 (FIXED)	1.94
75	244.456±0.16	2.80 (FIXED)	1.18
85	244.599±0.13	2.80 (FIXED)	1.29

Average Beam Momentum = 244.594±0.037 MeV/c

Average Beam Width = 2.71±0.05 MeV/c

Table III-3

Calculated Centroids of Gaussian Peaks and Quasi-Elastic Upper Limit

Lab Angle (°)	Carbon Elastic	Carbon Inelastic - 4.43 MeV	Carbon Inelastic - 9.64 MeV	Carbon Quasi-Elastic	Proton Elastic
35°	241.8	236.7	230.6	222.0	230.1
40°	241.6	236.5	230.4	221.8	226.7
45°	240.7	235.6	229.5	220.9	222.5
50°	240.9	235.8	229.8	221.2	219.0
55°	239.9	234.8	228.8	220.2	214.3
60°	240.0	234.9	228.9	220.3	210.4
65°	238.9	233.8	227.8	219.2	205.5
70°	238.9	233.8	227.8	219.2	201.5
75°	238.3	233.2	227.2	218.7	197.1
85°	237.4	232.4	226.4	217.9	188.6

The above values are calculated from the beam momenta listed in Table III-1

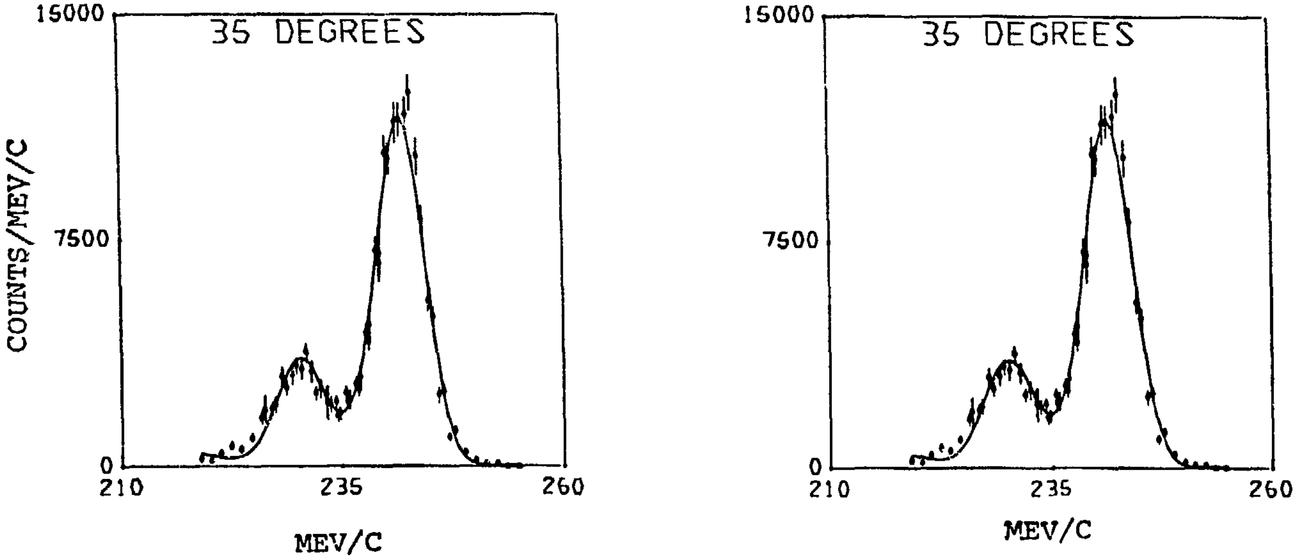

(a) (b)

FIGURE III-2. FITS TO THE 35° SPECTRUM. FIGURE III-2(a) IS THE FIT OBTAINED WITH THE SILBAR-STERNHEIM MODEL OF THE QUASI-ELASTIC BACKGROUND. FIGURE III-2(b) IS THE FIT OBTAINED WITH THE STEP FUNCTION MODEL OF THE QUASI-ELASTIC BACKGROUND.

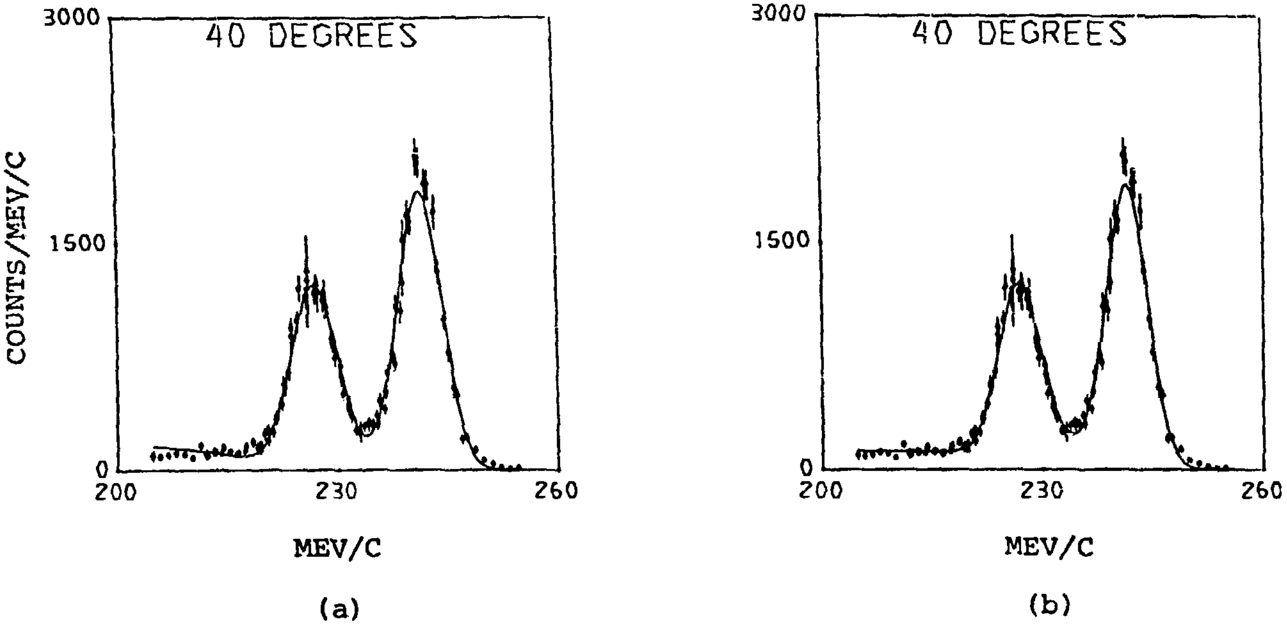

(a)

(b)

FIGURE III-3. FITS TO THE 40° SPECTRUM. FIGURE III-3(a) IS THE FIT OBTAINED WITH THE SILBAR-STERNHEIM MODEL OF THE QUASI-ELASTIC BACKGROUND. FIGURE III-3(b) IS THE FIT OBTAINED WITH THE STEP FUNCTION MODEL OF THE QUASI-ELASTIC BACKGROUND.

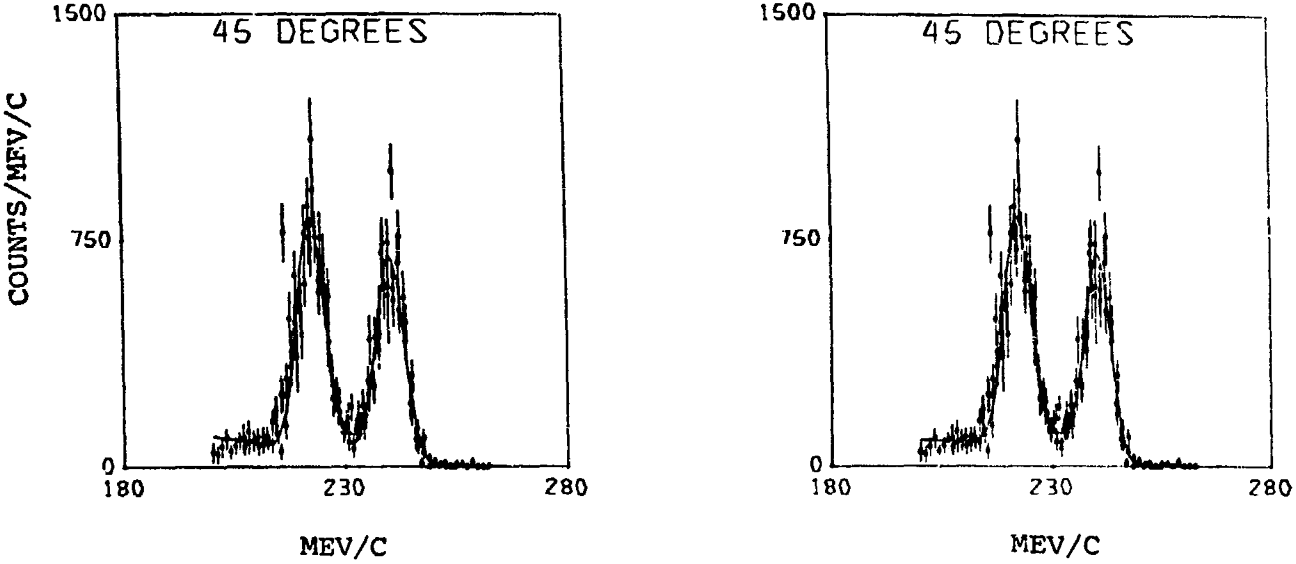

(a) (b)

FIGURE III-4. FITS TO THE 45° SPECTRUM. FIGURE III-4(a) IS THE FIT OBTAINED WITH THE SILBAR-STERNHEIM MODEL OF THE QUASI-ELASTIC BACKGROUND. FIGURE III-4(b) IS THE FIT OBTAINED WITH THE STEP FUNCTION MODEL OF THE QUASI-ELASTIC BACKGROUND.

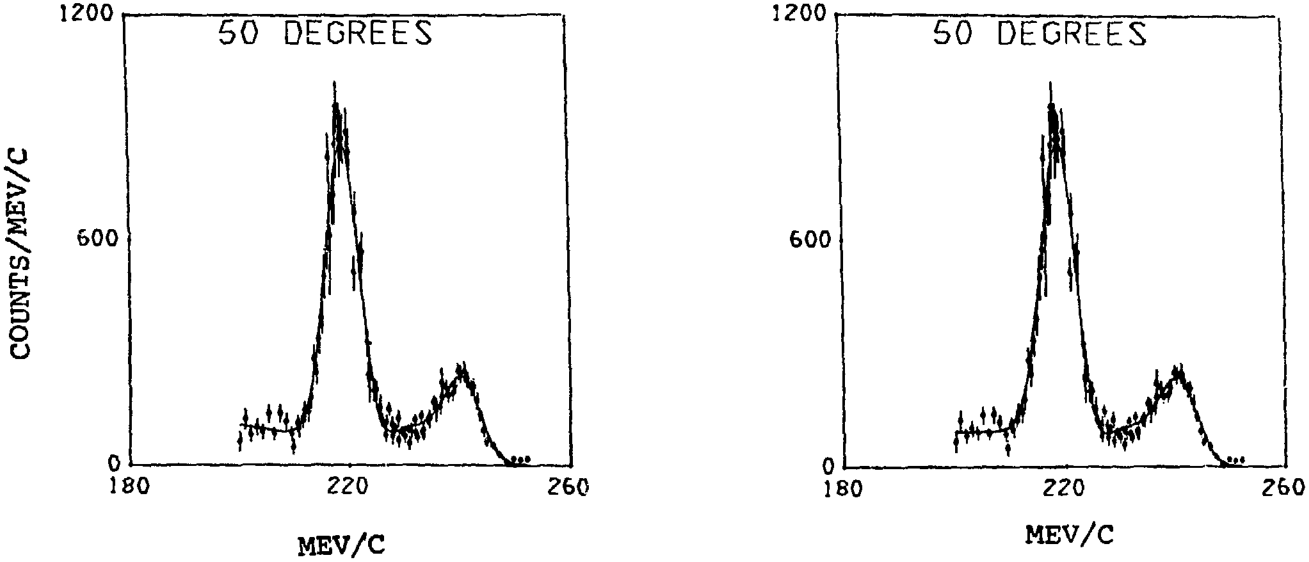

(a)

(b)

FIGURE III-5. FITS TO THE 50° SPECTRUM. FIGURE III-5(a) IS THE FIT OBTAINED WITH THE SILBAR-STERNHEIM MODEL OF THE QUASI-ELASTIC BACKGROUND. FIGURE III-5(b) IS THE FIT OBTAINED WITH THE STEP FUNCTION MODEL OF THE QUASI-ELASTIC BACKGROUND.

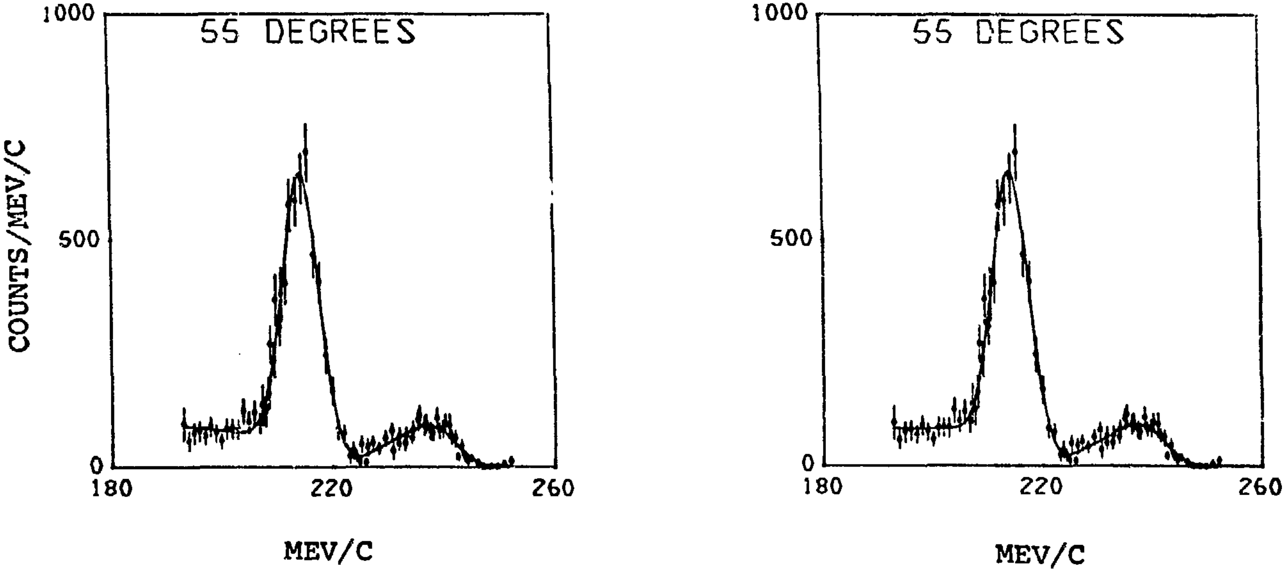

(a) (b)

FIGURE III-6. FITS TO THE 55° SPECTRUM. FIGURE III-6(a) IS THE FIT OBTAINED WITH THE SILBAR-STERNHEIM MODEL OF THE QUASI-ELASTIC BACKGROUND. FIGURE III-6(b) IS THE FIT OBTAINED WITH THE STEP FUNCTION MODEL OF THE QUASI-ELASTIC BACKGROUND.

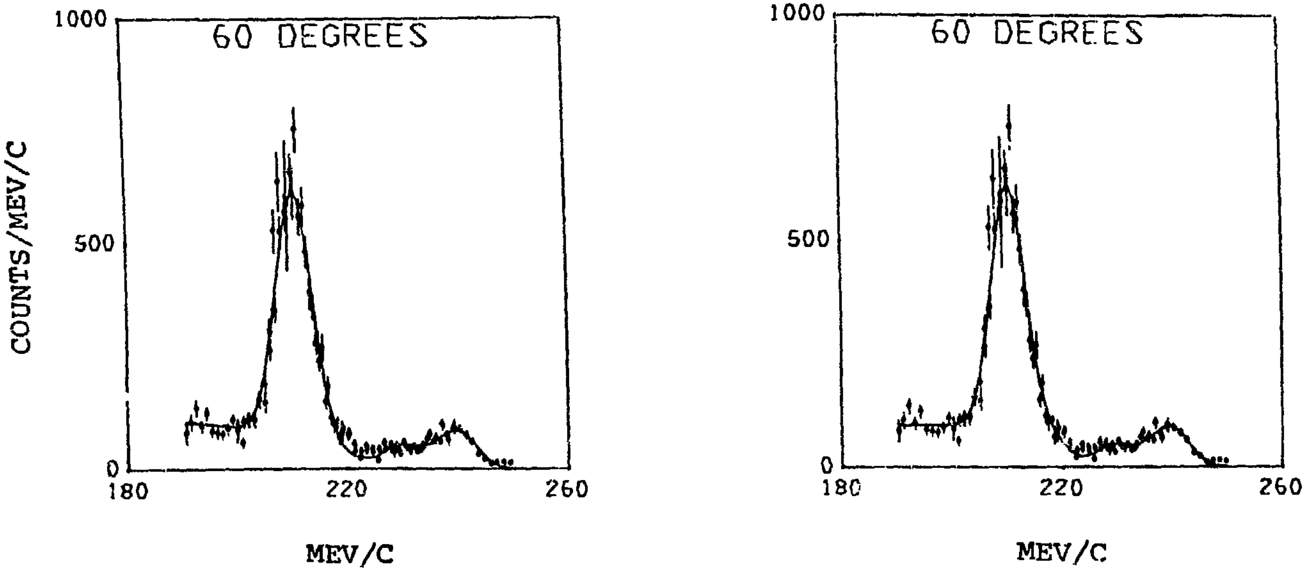

(a) (b)

FIGURE III-7. FITS TO THE 60° SPECTRUM. FIGURE III-7(a) IS THE FIT OBTAINED WITH THE SILBAR-STERNHEIM MODEL OF THE QUASI-ELASTIC BACKGROUND. FIGURE III-7(b) IS THE FIT OBTAINED WITH THE STEP FUNCTION MODEL OF THE QUASI-ELASTIC BACKGROUND.

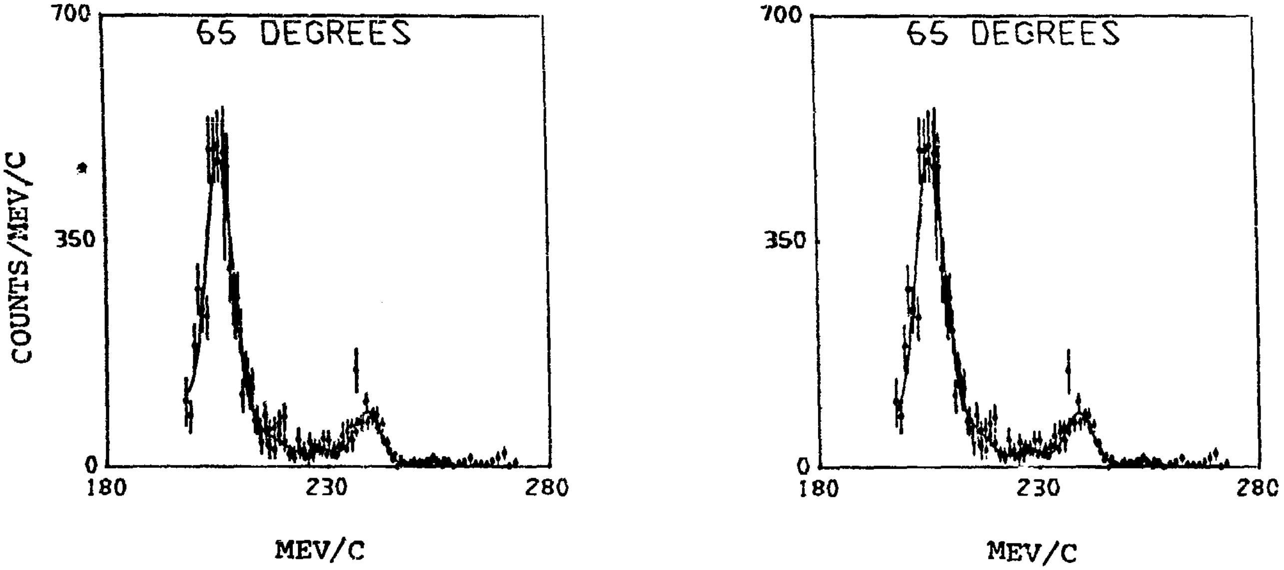

(a) (b)

FIGURE III-8. FITS TO THE 65° SPECTRUM. FIGURE III-8(a) IS THE FIT OBTAINED WITH THE SILBAR-STERNHEIM MODEL OF THE QUASI-ELASTIC BACKGROUND. FIGURE III-8(b) IS THE FIT OBTAINED WITH THE STEP FUNCTION MODEL OF THE QUASI-ELASTIC BACKGROUND.

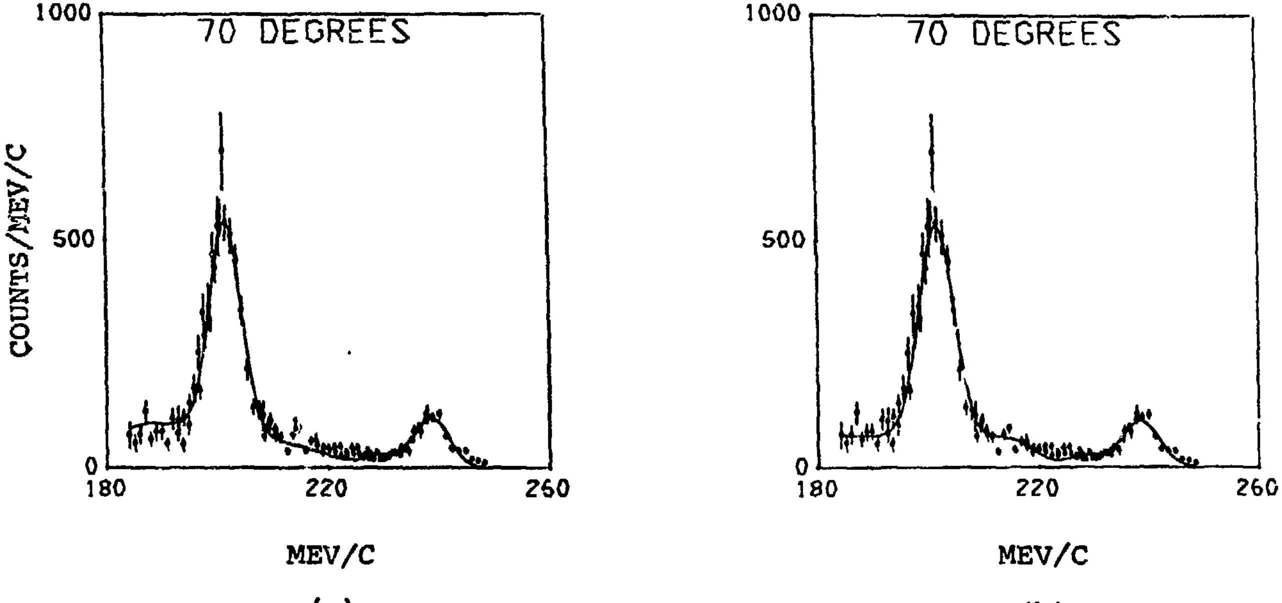

(a) (b)

FIGURE III-9. FITS TO THE 70° SPECTRUM. FIGURE III-9(a) IS THE FIT OBTAINED WITH THE SILBAR-STERNHEIM MODEL OF THE QUASI-ELASTIC BACKGROUND. FIGURE III-9(b) IS THE FIT OBTAINED WITH THE STEP FUNCTION MODEL OF THE QUASI-ELASTIC BACKGROUND.

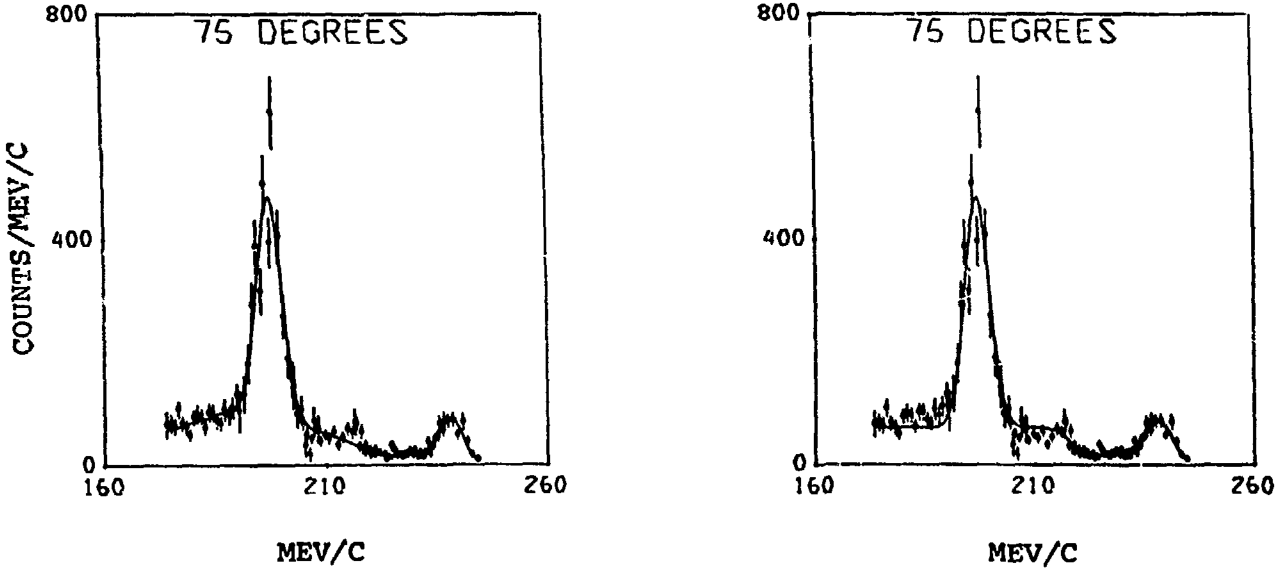

(a) (b)

FIGURE III-10. FITS TO THE 75° SPECTRUM. FIGURE III-10(a) IS THE FIT OBTAINED WITH THE SILBAR-STERNHEIM MODEL OF THE QUASI-ELASTIC BACKGROUND. FIGURE III-10(b) IS THE FIT OBTAINED WITH THE STEP FUNCTION MODEL OF THE QUASI-ELASTIC BACKGROUND.

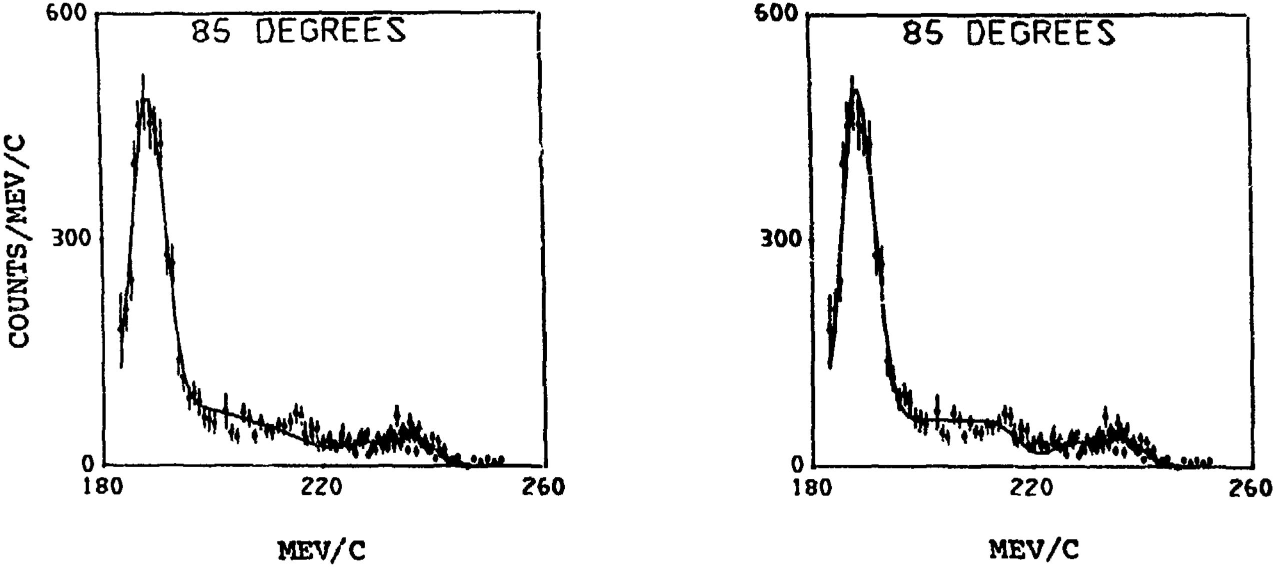

(a) (b)

FIGURE III-11. FITS TO THE 85° SPECTRUM. FIGURE III-11(a) IS THE FIT OBTAINED WITH THE SILBAR-STERNHEIM MODEL OF THE QUASI-ELASTIC BACKGROUND. FIGURE III-11(b) IS THE FIT OBTAINED WITH THE STEP FUNCTION MODEL OF THE QUASI-ELASTIC BACKGROUND.

the ion chamber. Although the absolute calibration was altered, this experiment required only the normalization to be constant over the data collection runs at each angle. However, the normalization was now sensitive to the steering of the beam. To correct the deviation the normalizations of two of the three sets of 19 data were incorporated into the fit as free parameters.

At 35° and 40° the fitting algorithm cound not separate the proton elastic from the 9.64 MeV carbon inelastic level. The separation of the centroid of the two peaks was 0.5 MeV/c at 35° and 3.7 MeV/c at 40°, while the width of each peak was approximately 2.8 MeV/c. The cross section for the 9.64 MeV level, exptrapolated from the fits at larger angles, was estimated to be 1.5±0.3 mb/sr at both angles, and incorporated into the fit as fixed parameters.

The initial fits to the 70° and 75° spectra produced a zero value for the 4.43 MeV inelastic cross section and a beam dispersion inconsistently larger than at other angles. The beam width tended to be broad at the larger angles because neither of the quasi-elastic functions were the true model of the data, although both were good approximations. At 70° and 75° the beam width was further increased by the poorly defined carbon elastic and 4.43 inelastic peaks (Figs. III-9 and III-10). Thus, the fit could be improved by making either the beam width

Table III-4

π^+p Elastic Scattering from Liquid Hydrogen Target

Lab Angle (Degrees)	Beam Momentum (MeV/c)	Beam Width (MeV/c)	χ^2/N_D
36.7	246.32±0.08	1.91±0.06	1.28
50.0	246.26±0.07	1.90±0.05	0.57
65.0	246.22±0.09	1.87±0.09	0.95
80.0	246.00±0.09	2.10±0.53	0.80
95.0	246.41±0.13	1.96±0.07	1.69
110.	246.45±0.11	1.93±0.05	0.84

or the 4.43 inelastic cross section a fixed parameter. The fits at smaller angles and the measurements of Binon et al (BI70) for $\pi^- + {}^{12}C$ suggested the 65° to 75° region contained the first diffraction minima for the 4.43 MeV inelastic channel, thus making the cross section small and difficult to determine. An estimation based upon the results of Binon et al was at best uncertain, because the diffraction minima occurred at smaller angles for π^- scattering than for π^+ scattering. Extrapolating the 4.43 MeV inelastic cross sections from the fits at smaller angles of this experiment still produced insonsistently large beam widths (2.9 to 3.1 MeV/c). However, the model dependence of the carbon elastic cross section was slight, being one half of a standard deviation larger for the fits using the statistical model than for the step function model. The fitting difficulty was overcome by extrapolating the beam dispersion from smaller angles and making it a fixed parameter.

Finally, the 85° spectrum was difficult to fit because insufficient data were collected on the low momentum side of the proton peak. Thus, the peak's centroid and width were poorly defined, resulting in a solution whose beam dispersion was inconsistently larger than at other angles. To eliminate this incongruity, the beam dispersion was extrapolated from the results at other angles and made a fixed parameter.

An evaluation of the beam momentum and dispersion as a function of angle provides insight into the adequacy of the kinematical corrections and the consistency of the beam tune. The results for either model of the quasi-elastic background showed a slight systematic difference in the beam momentum between the even and odd angles, which was a consequence of the pion beam channel being turned off and reset between the time the two sets of data were taken. That the difference was small demonstrated the consistency and the ability to reset the pion channel. Also, the measured beam momentum was about 2% lower than the value used in setting up the pion channel suggesting a slight shift in the calibration of the channel's magnets. Results shown in Table III-4, from another experiment, which was identical except for the substitution of a liquid hydrogen target and the setting of the last four quadrupole magnets which affect only the beam spot size, support this 2% discrepancy. The data were fit to a constant plus a Gaussian whose centroid and width were coupled to the beam momentum and beam width using an identical procedure as described in the present Chapter. The free parameters were the beam momentum width, the beam momentum, the area, and the constant background.

A correlation was evident as the parameter representing the beam momentum width displayed a systematic variation with angle instead of having a random scatter about some mean value. This correlation could be explained in terms of a yet unknown physical effect or, more likely, an inadequacy in one or more assumptions used to fit the data. For example, it was assumed the contributions to the widths were independent and could be added in quadrature. An alternative would be a simple sum, but this assumption led to negative widths. Some of the correlation appeared to have arisen from the approximations to the quasi-elastic background, as mentioned earlier. Coupling the centroid and width of the proton peak to the beam parameters, independently of the carbon peaks, demonstrated the peak with the larger amplitude had the greatest influence in determining the beam dispersion. Thus, at the larger angles the beam width was directly affected by the proton peak and indirectly by the approximation to the quasi-elastic background underneath. Nevertheless, the correlation was small, and the χ^2/N_D demonstrated that reasonable fits were obtained.

Of the two models used for the quasi-elastic background, both were reasonable representations of the data and produced similar cross sections. At 35° through 45°, where there was little contribution from the quasi-elastic background to the proton peak, the difference between the cross sections produced by both models was insignificant. At larger angles, the two cross sections differed on the average by about half of a standard deviation. The difference between the χ^2/N_D produced by both models were statistically insignificant at each angle; however, the step function model produced slightly lower values at most angles. Inspection of the lower momentum portions of Figs. III-2 through III-11 suggests the step function was the closer approximation to the quasi-elastic background except at 75°. Although one would have hoped the better fit to have come from the statistical model, several simplifying assumptions made in the model of Silbar and Sternheim (SS76) such as neglecting nuclear structure and multiple scattering processes were not entirely valid. Although the difference between the two models was slight, the step function appeared to better fit the data, and its results were used to calculate the cross sections as discussed in the next chapter.

CHAPTER IV

RESULTS AND CONCLUSIONS

Introduction

In previous chapters a methodology for this experiment was presented, the equipment was described, and the fitting of a theoretical function to the data was detailed and discussed. The result was the determination at ten laboratory angles of the areas of two scattering peaks, one representing elastic scattering from carbon and the other representing elastic scattering from protons. This chapter will show the transformation from these areas into the carbon differential cross section. Finally these cross sections will be compared with similar measurements of the reaction $\pi^- + {}^{12}C$ as reported by Binon et al (BI70).

Determination of the Cross Section

The determination of the carbon elastic cross section in the CM system involved the measurement of the $\pi^+ + p$ elastic cross section by Bugg et al (BB73) as well as the ratio of the carbon elastic to proton elastic cross sections as determined by this experiment. These cross sections were given by:

$$d\sigma_i/d\Omega = A_i E_i J_i/(\Gamma \cdot \Lambda \cdot \Delta\Omega)$$

in which A_i is the area of the Gaussian peak representing the ith channel, E_i is the correction for pion decay, J_i is the Jacobian, Γ is a factor representing the target's size, shape, and density, Λ is the number of incident pions, and $\Delta\Omega$ is the angular acceptance of the spectrometer. The correction for pion decay between the target and the detectors was:

$$E_i = \exp[-\lambda M_\pi/(\tau c \cdot p_i)]$$

in which the pion decay constant τc is 780.4 cm. The path length, λ, and the momentum, p_i, were reasonably approximated by the central path length of the spectrometer and the momentum of the scattered pion as calculated from the kinematics. The term J_i is the Jacobian which effects the transformation from the laboratory system to the CM system and involves only $\cos\theta$ since the coordinate ϕ and the number of scattered pions are invariants. Thus, for the ith channel:

$$J_i = \left|\frac{d\cos\theta}{d\cos\theta^*}\right| = |p_i^* M_\pi^{-3}(T_i T_i^* - \gamma M_\pi^2)|$$

in which T_i is the kinetic energy of the pion and the asterisk refers to the CM system. The remaining terms in the cross section formula were independent of the scattering channel and thus canceled in the ratio of cross sections. Explicitly, this ratio as determined by this experiment was:

$$(d\sigma_C/d\Omega)/(d\sigma_p/d\Omega) = R_{Cp}(A_C E_C J_C)/(A_p E_p J_p)$$

in which R_{Cp} is the ratio of the number of carbon nuclei to the number of free protons in the target.

The $\pi^+ + p$ cross sections of Bugg et al (BB73) were phase shift analyzed by Carter et al (CA73). Carter's results for the T = 3/2 channel at 142.9 MeV were extrapolated to beam energy found by the fitting algorithm, and the $\pi^+ + p$ elastic differential cross section was calculated for the required scattering angles. Only the s, p, d, and f waves were significant at this energy. The cross section's variance was determined from an error matrix that was generated from the phase shift analysis (BU75).

One final adjustment to the cross sections corrected for the variation of the cross section with angle across the spectrometer entrance. In effect this variation introduced a small shift in the angle at which the spectrometer observed the target, an effect similar to, but independent of the correction p_{ang} described in the previous chapter. Although this effect was negligible for the proton cross section, it must be considered when calculating the carbon elastic cross section. The correction was expressed as a ratio of uncorrected to corrected cross sections, and a third order Taylor's expansion about $\cos\theta_L$ was made. The first through third derivatives of the carbon cross sections were determined from the solution of the optical model discussed in the next section. The terms involving $\overline{(\cos\theta - \cos\theta_L)^n}$ were the averages calculated in the Monte Carlo simulation of the target described in Chapter III. The results, the uncorrected cross sections, the geometric correction, and the corrected cross section are shown in Table IV-1. The fits to the optical model discussed in the next section were made with the corrected cross sections.

The fractional error of the final carbon elastic cross section was the square root of the sum of the squares of the fractional errors of the experimentally determined carbon elastic cross section, the experimentally determined proton cross section, the ratio of the number of carbon nuclei to free protons in the target, and the proton cross section determined from Carter's phase shift analysis.

Table IV-1

$\pi^+ + {}^{12}C$ Differential Elastic Cross Sections

CM Angle (°)	Uncorrected Cross Section (mb/sr)	Geometric Correction	Corrected Cross Section (mb/sr)
35.82	65.9 ±5.2	0.999	65.8 ±5.2
40.92	25.95±0.96	0.984	25.54±0.95
46.01	12.10±0.78	0.959	11.60±0.75
51.09	3.27±0.20	0.921	3.01±0.18
56.17	1.16±0.12	0.922	1.07±0.11
61.24	1.42±0.12	0.989	1.40±0.12
66.29	1.72±0.16	1.013	1.74±0.16
71.34	1.87±0.14	1.014	1.90±0.14
76.37	1.54±0.16	1.008	1.55±0.16
86.42	0.57±0.06	0.990	0.57±0.06

Average Beam Kinetic Energy = 142.036±0.031 MeV

Cross Sections and Optical Model

The results for the elastic cross sections are presented in Table IV-1 and Figure IV-1. The published values of Binon et al (BI70) are plotted in Figure IV-2. Although their beam momentum was 7% greater than that of this experiment, both measurements were at the broad (3,3) resonance (SS74), inviting comparison of the two sets of data by fitting the cross sections to a solution of the Klein-Gordon equation using an adjustable optical model potential. A computer program, FITPI, (CE75) offers the user a choice of several potentials and performs a least squares fit to the input using a partial wave expansion.

The nucleus was described by a charge distribution and a matter distribution which for ^{12}C were taken to be the same. Electron-carbon scattering experiments demonstrated the charge distribution was a modified Gaussian (LB67):

$$\rho_C(r) = 2e(\sqrt{\pi}\, R_C)^{-3} \exp[-(r/R_C)^2]\cdot[1 + (z - 2) \cdot (r/R_C)^2/3]$$

in which R_C is the charge radius of ^{12}C. A modified Gaussian matter distribution was used with the matter radius, R_M, replacing R_C in the above equation. Both R_M and R_C are calculated from the rms radius of the charge density, $a = 2.45$ f, listed in de Jager et al (DE74)

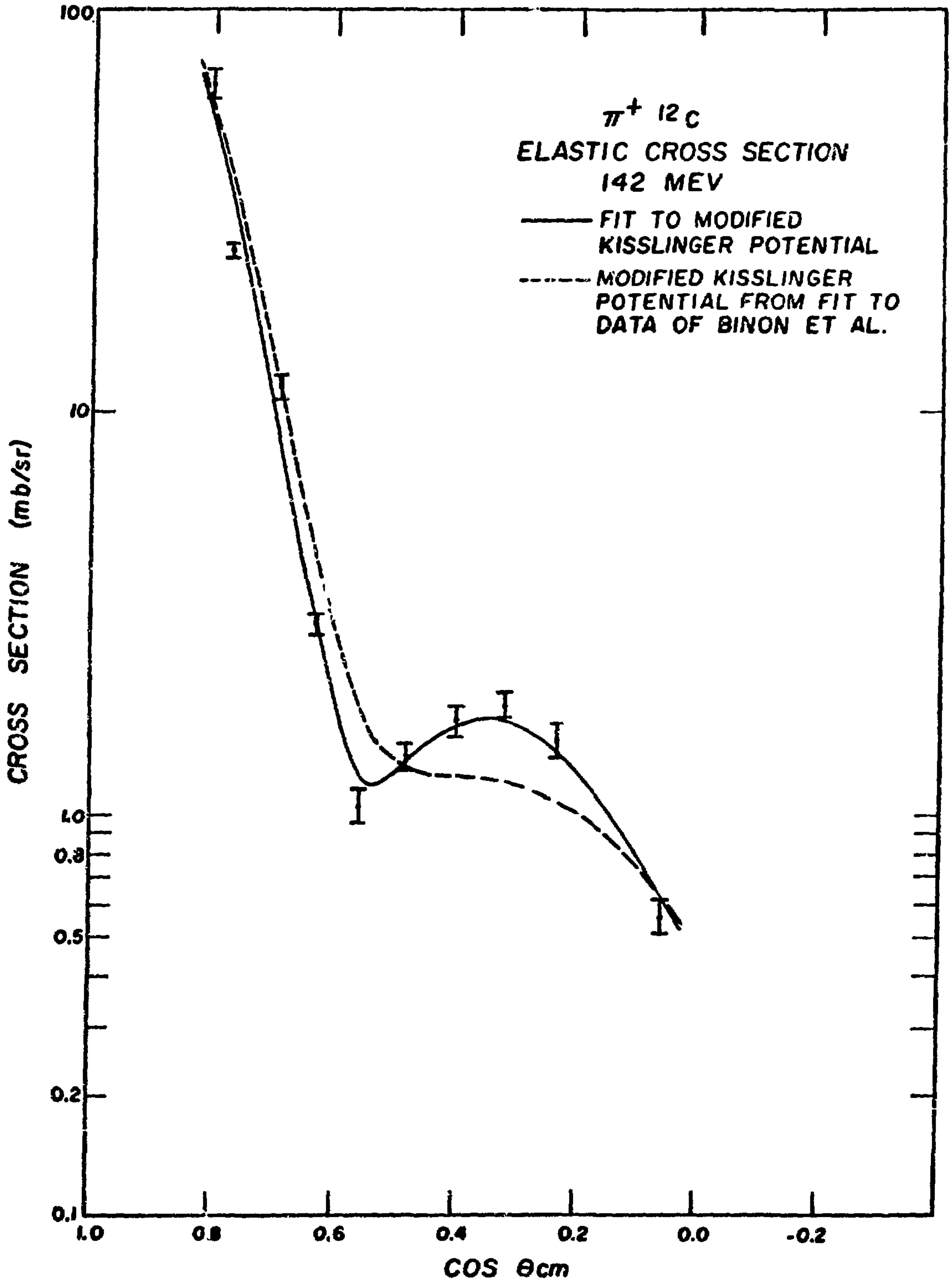

π^+ ^{12}C
ELASTIC CROSS SECTION
142 MEV
FIT TO MODIFIED KISSLINGER POTENTIAL
MODIFIED KISSLINGER POTENTIAL FROM FIT TO DATA OF BINON ET AL.
CROSS SECTION (mb/sr)
100
10
1.0
0.8
0.5
0.2
0.1
1.0
0.8
0.6
0.4
0.2
0.0
-0.2
COS θcm

FIGURE IV-1.

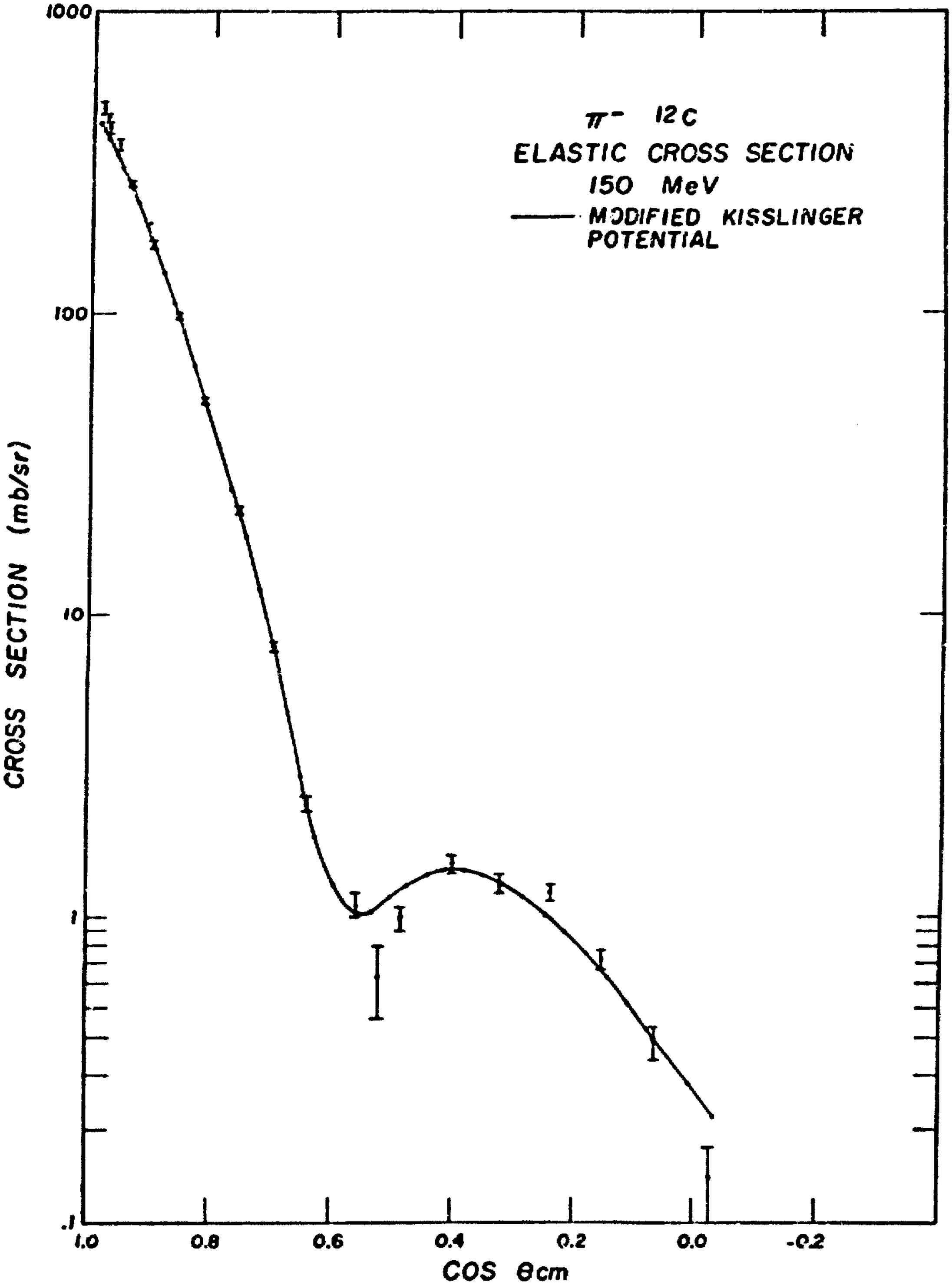

π⁻ 12C
ELASTIC CROSS SECTION
150 MeV
MODIFIED KISSLINGER POTENTIAL
CROSS SECTION (mb/sr)
1000
100
10
1
.1
1.0
0.8
0.6
0.4
0.2
0.0
-0.2
COS θcm

FIGURE IV-2.

which is slightly different from the previous value of Hofstader (LB67). For this particular program:

$$R_C = (a^2 + r_\pi^2)^{1/2}/k = 1.73 \text{ f}$$

and:

$$R_M = (a^2 - r_p^2)^{1/2}/k = 1.57 \text{ f}$$

in which the pion charge radius, r_π, is 0.71 f (AD74), the proton charge radius is 0.80 f (DE74) and $k = (13/6)^{1/2}$ (LB67). Eleven partial waves were used. All ten data points of this experiment were used in the fit, but only the twenty data points forward of 95° were used in the fits to the π^- data.

Elastic scattering in this energy range is thought to be dominated by the (3,3) resonance (SS74). Kisslinger introduced a nonlocal potential which includes a p-wave contribution to the pion-nucleon interaction (KI55). In coordinate space the Kisslinger potential is:

$$V_K(r) = -A[k^2 b_o \rho(r) + b_1 \vec{p}\cdot\rho(r)\vec{p}]$$

in which the momentum operator is $\vec{p} = -i\vec{\nabla}$. Because of the gradient term, this model is sensitive to surface effects. Miller (MI74) and Tabakin and Kisslinger (KT74) modified the above potential by including the Fermi motion of the nucleons, resulting in a third term. The modified Kisslinger potential is:

$$V_{MK}(r) = V_K(r) - A\, b_1 (T^* + M_\pi)/(2M_N)\ \nabla^2 \rho(r)$$

in which T* is the CM kinetic energy.

The results of the best fits to the optical model are displayed in Table IV-2 and in Figs. IV-1 and IV-2. The magnitude of b_1 demonstrates strong p-wave scattering and the dominance of the (3,3) resonance while the magnitude of the imaginary parts shows strong scattering into inelastic channels. A comparison of the parameters for the best fits of the Kisslinger potential with those of the modified Kisslinger potential shows the correction for the Fermi momentum is significant. However, the difference between the cross sections calculated from the potentials in each case is slight, and when plotted, the curve generated by the Kisslinger potential appeared identical to the curve generated by the modified Kisslinger potential. As a curiosity, the π^- modified Kisslinger potentials in Table IV-2 were used to generate the π^+ cross sections at 142 MeV, represented by the dashed curve in Fig. IV-1. The failure to reproduce the data was not surprising because Im b_o, and Re b_1, of the π^+ potentials, were significantly different from those of the π^- potentials.

The potentials failed to accurately reproduce the diffraction minima as can be seen in the illustrations. Both sets of data indicated the minima were deeper and at slightly different angles from the

Table IV-2

Optical Model Results for ^{12}C

	Kisslinger Potential		Modified Kisslinger Potential	
π^+	Re b_o	-4.16±2.99	Re b_o	-4.39±2.52
	Im b_o	2.44±2.19	Im b_o	3.78±1.95
	Re b_1	5.33±4.25	Re b_1	3.74±2.72
	Im b_1	12.3±2.49	Im b_1	9.82±2.22
	χ^2/N_D	3.25	χ^2/N_D	3.64
π^-	Re b_o	-4.26±0.15	Re b_o	-4.65±0.13
	Im b_o	0.62±0.18	Im b_o	1.59±0.17
	Re b_1	3.32±0.30	Re b_1	2.38±0.27
	Im b_1	12.3±0.25	Im b_1	10.3±0.25
	χ^2/N_D	3.08	χ^2/N_D	3.08

The units of the potential's parameters are Fermi^3.

cross sections calculated from the optical model. The optical model demonstrates that identical failings characterized the fitting of the π^+ and π^- cross sections, thus showing the results of this experiment were not inconsistent with the results of Binon et al (BI70).

Summary and Conclusions

In summary, this dissertation has described and discussed the measurement of the $\pi^+ + {}^{12}C$ elastic differential cross section at 142 MeV, a study undertaken with two goals in mind: 1) to measure a reaction in an energy range where no previous measurement exists, and 2) to provide a means of calibrating and understanding the experimental apparatus so it may be used in future experiments. A pion beam generated in the P^3 experimental area of LAMPF was incident upon a styrofoam $(CH)_n$ target. A magnet spectrometer provided angle and momentum analysis of the scattered pions. The spectrometer was rotated to one of ten angles, and data were collected at several different settings of the spectrometer's central momentum. The resulting data at each angle were properly normalized and merged into a momentum spectrum of the proton elastic scattering peak, the carbon elastic peak, several carbon inelastic peaks, and the upper momentum portion of the broad distribution resulting from quasi-elastic scattering in carbon. These spectra were fit with a set of kinematically coupled Gaussians and one of two functions representing the quasi-elastic background. The fitted areas of the peaks corresponding to carbon elastic and proton elastic scattering with proper transformations defined the ratio $(d\sigma_C/d\Omega)_{CM}/(d\sigma_p/d\Omega)_{CM}$. This ratio was normalized to the $\pi^+ + p$ elastic cross sections of Bugg et al (BB73) to establish the value of $d\sigma_C/d\Omega$. A fit was made to the optical potential model in order to estimate a small geometrical correction to the cross sections and to determine if the results were consistent with a similar conjugate measurement of Binon et al (BI70).

There are several conclusions one may draw from this work. It has been shown through the discussions of the experimental method, the equipment, and the data analysis that the results of this experiment were reliable and not inconsistent with the results of Binon et al. Also, the optical model reproduced the general trend of the data, for both π^+ and π^-, although failing to correctly reproduce the diffraction minima. Finally, the experimental technique was sound, and the necessary calibrations for future experiments were made.

It is anticipated that similar experiments will follow as the number of facilities for creating intense pion beams increases. Performing experiments of this type with greater resolution would permit the measurement of inelastic cross sections for a variety of nuclei over a wider energy range thus generating an abundance of data to provide insight into several theoretical areas. For example, it is clear the Kisslinger models are capable of qualitative fits to the data over this energy range, but improvements are needed if quantitative fits are to be obtained. In short, the picture of the nucleus and of nuclear interactions is by no means complete. It is hoped that this experiment, and others like it, will help to make our understanding more complete.

ACKNOWLEDGMENTS

I wish to thank the Physics Department, the University of Wyoming, and the Los Alamos Scientific Laboratory for the facilities and services they have provided over the course of my graduate education. Special thanks are due to Dr. Charles Bordner, Dr. Peter Gram, Dr. Kenneth Johnson, Dr. Ray Kunselman, Dr. Lee Schick, Dr. Frank Shively, and Dr. Ray Smith for many valuable and interesting discussions. I thank John Walter for his assistance, especially with computer programming. I wish to thank my advisor, Dr. Glen A. Rebka, Jr. for his guidance and support during the time I have been working on this problem.

REFERENCES

(AD74) G.T. Adylov, F.K. Aliev, D.Yu. Bardin, W. Gajewski, I. Ion, B.A. Kulakov, G.V. Micelmacher, B. Niczyporuk, T.S. Niganov, E.N. Tsyganov, M. Turala, A.S. Vodopianov, K. Wala, E. Dally, D. Drickey, A. Liberman, P. Shepard, J. Tomkins, C. Buchanan, J. Poirier; Phys. Lett. 51B(1974) 402.

(BB73) D.V. Bugg, P.J. Bussey, A.A. Carter, J.R. Carter D.R. Dance, A.M. Smith; Nucl. Phys. B58(1973)363.

(BI70) F. Binon, P. Duteil, J.P. Garron, J. Gorres, L. Hugon, J.P. Peigneux, C. Schmidt, M. Spighel, J.P. Stroot; Nucl. Phys. B17(1970)168.

(BR67) K.L. Brown; "A First and Second Order Matrix Theory for the Design of Beam Transport Systems and Charged Particle Spectrometers", SLAC-75 (1967).

(BU75) D.V. Bugg; Private Communication, 1975.

(CA73) J.R. Carter, D.V. Bugg, A.A. Carter; Nucl. Phys., B58(1973)378.

(CE75) M.D. Cooper, R.A. Eisenstein; LA-5929-MS.

(DE74) C.W. de Jager, C. de Vries, E. de Vries; Atomic and Nuclear Data Tables, Vol. 14, Nos. 5,6 1974.

(FA72) G. Fäldt; Phys. Rev. C5(1972)400.

(GR71) B. Grennberg, A. Rytz; Metrologia 7(1971)65.

(JA65) J. Jani; Air Force Weapons Laboratory-TR-65-150.

(KI55) L.S. Kisslinger; Phys. Rev., 98(1955)761.

(KO70) D.S. Koltun; "Interactions of Pions with Nuclei", Adv. Nucl. Phys. Vol. 3(Academic Press, NY, 1970).

(KT74) L.S. Kisslinger, F. Tabakin; Phys. Rev. C9(1974) 188.

(LB67) H.R. Collard, L.R.B. Elton, R. Hofstader, H. Schopper; Landolt-Börnstein Numerical Data and

Functional Relationships in Science and Technology, edited by K.H. Heilwege, Springer-Verlag, Berlin(1967), New Series, Group 1, Vol. 2.

(LI76) M. Sternheim, E. Auerbach; Phys. Rev. Lett. 25(1970)1500; M. Krell, S. Barmo; Nucl. Phys. B20(1970)461: G.W. Edwards, E. Rost; "π-Carbon Inelastic Scattering Near the 3-3 Resonance", Preprint, (1971); K. Bjϕrnenak, J. Finjord, P. Osland, A. Reitan; Nucl. Phys. B22(1970) 179; C. Wilkin; Nuovo Cim. Lett., 4(1970)491; C. Schmidt; Nuovo Cim. Lett., 4(1970)454.

(MI74) G.A. Miller; Phys. Rev., C10(1974)1242.

(RO61) B. Rossi; High Energy Particles, Prentice Hall, 1961.

(SE53) E. Segrè; Experimental Nuclear Physics, John Wiley & Sons, 1953.

(SS74) M.M. Sternheim, R.R. Silbar; Annual Review of Nuclear Physics, Vol. 24(1974)249.

(SS76) R.R. Silbar; Private Communication, 1976.

(ST56) R.M. Sternheimer; Phys. Rev. 103(1956)511.

(ST59) R.M. Sternheimer; Phys. Rev. 115(1959)137.

(TH70) H. Thiessen, S. Sobottka; "A Proposal for EPICS", LASL Report #LA-4534-MS, 1970.

(TR57) H.F. Trotter; "Gauss' Work (1802-1826) on the Theory of Least Squares", an English translation, AEC-TR-3049(1957).

(TR74) H.J. Trussel; Private Communication, 1975.

APPENDIX A

DEFINITION OF SELECTED VARIABLES

E_b = Total energy of pion beam

E_i = Total energy of scattered pion

E_T = Total energy of pion-nucleus system

e = Charge of the electron

i = Channel index of scattered pion

M_e = Mass of the electron

M_i = Mass of the nucleus after scattering

M_N = Mass of the nucleus before scattering

M_π = Mass of the pion

p_b = Momentum of the pion beam

p_i = Momentum of the scattered pion calculated from kinematics

r_e = Classical radius of the electron

S_{in} = Path length of pion into the target before scattering

S_{out} = Path length of pion out of the target after scattering

T_b = Kinetic energy of the pion beam

T_i = Kinetic energy of scattered pion

v = Velocity of pion beam

z = Number of electrons per target molecule

β = Velocity of the CM system divided by the speed of light

$\gamma = (1 - \beta^2)^{-1/2}$

δ = Spectrometer dispersion

θ = Scattering angle

θ_L = Nominal Laboratory scattering angle

μ_i = Mean momentum of scattered pions

ρ = Target density

σ_b = Beam's momentum dispersion

σ_i = Width of the Gaussian scattering peak or broadening of the quasi-elastic transition

* = Quantity is evaluated in the CM system

APPENDIX B

MAGNET EXCITATION FUNCTION

The central fields of the spectrometer magnets were separately measured as a function of driving current. This driving current is measured as a voltage drop across a series resistance. The data of these measurements were approximated by an integrated Fermi distribution. Like the excitation curve it reproduces, this function is almost linear to a point and then saturates. A polynomial could produce good fits at data points, but would have undesirable curvature between the data points. Thus, the integrated Fermi distribution is preferred.

The basic definition of the distribution is:

$$f(\varepsilon) = \{1 + \exp[(\varepsilon-\mu)/\sigma]\}^{-1},$$

in which ε is the independent variable, μ is the value of ε where f is 1/2 of its maximum value, and σ is the width of the transition region. The integrated distribution is:

$$F(x) = A + B[1 + \exp(-\mu/\sigma)]\int_0^x f(\varepsilon)\, d\varepsilon,$$

in which A is the y intercept and B is the slope of the function at $x = 0$. Realizing the $f(\varepsilon)$ may be expressed as:

$$f(\varepsilon) = \exp[(\mu-\varepsilon)/\sigma]/\{1 + \exp[(\mu-\varepsilon)/\sigma]\},$$

the following substitutions are made:

$$y = \exp[(\mu-\varepsilon)/\sigma],$$

and:

$$dy = -y/\sigma \; d\varepsilon.$$

Thus, the integral becomes:

$$F(x) = A + B\sigma[1 + \exp(-\mu/\sigma)]\int_0^x (1 + y)^{-1} \, dy$$

$$= A + B\sigma[1 + \exp(-\mu/\sigma)] \cdot \ln \{1 + \exp[\mu/\sigma]\}/\{1 + \exp[(\mu-x)/\sigma]\},$$

in which F is the central field in kG, x is the shunt voltage in mV, A is the y intercept, B is the slope of F at F(0), μ is the point of the roll off, and σ is the width of the roll off.

☆ U.S. GOVERNMENT PRINTING OFFICE: 1976—777-018/29